

ALMA MATER STUDIORUM · UNIVERSITÀ DI
BOLOGNA

Dipartimento di Fisica e Astronomia “Augusto Righi”
Corso di Laurea in Fisica

Facility for c-deuteron production in ALICE

Relatore:
Prof. Andrea Alici

Presentata da:
Giuseppe Luciano

Correlatore:
Dott. Nicolò Jacazio

Anno Accademico 2024/2025

Ringraziamenti

Un primo ringraziamento è rivolto al Prof. Andrea Alici e al Dott. Nicolò Jacazio che mi hanno pazientemente guidato in una delle fasi più importanti del mio percorso accademico e senza i quali questo lavoro non sarebbe stato possibile. Un grazie speciale è dedicato poi a tutti i compagni di viaggio, sia a chi mi è stato vicino nelle interminabili ore sui treni che a quelli che mi hanno accompagnato durante il percorso accademico. I primi sempre pronti ad ascoltarmi ed a ricordarmi che c'è tanto altro da imparare. I secondi invece mi hanno insegnato ad approcciarmi ad una disciplina tanto affascinante quanto ostica fungendo da inesauribile fonte di ispirazione nel mostrarmi i possibili modi di interfacciarsi alle difficoltà, ognuno con la propria strategia. Sono stati compagni di interminabili e stravagnati conversazioni dal moto caotico ed imprevedibile, perché spesso non lo si faceva per il risultato ma più per la genuina voglia di ragionare insieme. Sempre di fretta e sempre senza tempo eppure non si iniziava a lavorare seriamente senza prima aver proposto quell'improbabile argomento che ci bloccava per ore. Grazie ai miei grandi amici su cui ho sempre potuto contare anche se il tempo a loro dedicato non gli ha mai reso giustizia. A tutte quelle volte in cui non potevo uscire e a tutte le volte che mi hanno perdonato perché se ti presenti con una bottiglia di cola sarebbe semplicemente folle continuare a tenere il broncio. Un grazie anche alla mia ragazza che più di ogni altra persona sa quanti sacrifici sono stati necessari ed il cui supporto è stato indispensabile. Infine il pensiero principale è diretto ai miei genitori che anche se tornavo tardi avevano comunque la pazienza di aspettarmi per cena, che mi coccolavano nelle torride giornate di studio estivo con dell'acqua al limone ma nel bicchiere bello perché anche l'occhio vuole la sua parte, e che non potrò mai ringraziare abbastanza per tutti i sacrifici che hanno fatto per me.

Abstract

Recent developments in hadron spectroscopy, particularly in the charm sector, have revealed that there may exist different molecular bound states of hadrons, observed as hadron resonances. In particular, some studies suggest that the formation of molecules composed of particles containing a heavy quark is more plausible than we could have expected a few years ago. For this reason, this work explores the problem in more detail by focusing specifically on the c-deuteron, a super-nucleus consisting of a bound state between a Λ_c and a neutron. The Statistical Hadronisation Model was used to simulate the number of c-deuterons expected in a Pb-Pb collision as a function of various parameters. In particular it has been pointed out that the number of c-deuterons expected shows a cubic growth with the increase in the radius of the freeze-out surface. Performing a fit using the relation $dN/dy = ar^3 + b$, with a and b free parameters and r the radius, the results obtained are $a = (1.3921 \pm 0.0032) \cdot 10^{-6} fm^{-3}$, $b = (2.43 \pm 0.13) \cdot 10^{-8}$ with $\tilde{\chi}^2 = 0.42$.

For the increase in temperature, the functional relation that best described the data produced was of the form $dN/dy = ae^{bT} + c$, with a, b and c as fit parameters and T the temperature, the reason for this trend is unclear and might only reflect a local behavior of a more complex functional relation valid at a temperature around 156 MeV. The values obtained from the fit are $a = (1.19 \pm 0.17) \cdot 10^{-12}$, $b = (0.13009 \pm 0.00087) MeV^{-1}$ and $c = (-6.38 \pm 0.50) \cdot 10^{-6}$ with a $\tilde{\chi}^2 = 1.0$.

For the increase in charm fugacity, the relationship used for the fit was of the form $dN/dy = ax + b$ and the results obtained were $a = (2.366 \pm 0.032) \cdot 10^{-5}$, $b = (2.53 \pm 0.94) \cdot 10^{-5}$ and a $\tilde{\chi}^2 = 1.4$.

Dynamical simulations were then used to assess how the possible existence of this super-nucleus could increase the number of deuterons detected by the ALICE 3 detector. This value has been estimated under the following assumptions: the number of events generated by the LHC is 10^{10} ; only the central collisions were considered, assumed to be 5% of the total; only c-deuterons with $|y| < 0.5$ were considered, the freeze-out temperature was of 156 Mev, the freeze-out radius of 8 fm and charm fugacity of 29.6; only some decay channel has been considered. The resulting value is (1938 ± 12) deuterons. This value seems to indicate the real possibility of finding c-deuterons. However, given the unexpectedly high value, it remains possible that this state has not been observed because it does not form.

Abstract

Sviluppi recenti nella spettroscopia adronica hanno rivelato la possibile esistenza di diversi stati legati molecolari di adroni. Questo lavoro esplora il problema in modo più dettagliato, concentrandosi nello specifico sul c-deuterone, un super-nucleo costituito da uno stato legato tra una Λ_c e un neutrone. Per le analisi è stato utilizzato il Modello di Adronizzazione Statistica per simulare il numero di c-deuteroni attesi in collisioni Pb–Pb in funzione di vari parametri.

Si è osservato che il numero atteso di c-deuteroni mostra una crescita cubica con l'aumento del raggio della superficie di freeze-out. Effettuando un fit con la relazione $dN/dy = ar^3 + b$, con a e b parametri liberi e r il raggio, i risultati ottenuti sono: $a = (1.3921 \pm 0.0032) \cdot 10^{-6} \text{ fm}^{-3}$, $b = (2.43 \pm 0.13) \cdot 10^{-8}$, con $\tilde{\chi}^2 = 0.42$.

Invece la relazione funzionale meglio capace di descrivere i dati al variare della temperatura era della forma $dN/dy = ae^{bT} + c$, con a , b e c parametri di fit e T la temperatura. I valori ottenuti dal fit sono $a = (1.19 \pm 0.17) \cdot 10^{-12}$, $b = (0.13009 \pm 0.00087) \text{ MeV}^{-1}$ e $c = (-6.38 \pm 0.50) \cdot 10^{-6}$, con $\tilde{\chi}^2 = 1.0$.

Per quanto riguarda invece l'aumento della fugacità del charm, la relazione utilizzata per il fit è stata della forma $dN/dy = ax + b$, e i risultati ottenuti sono: $a = (2.366 \pm 0.032) \cdot 10^{-5}$, $b = (2.53 \pm 0.94) \cdot 10^{-5}$, con $\tilde{\chi}^2 = 1.4$.

Sono state poi condotte analisi sulla dinamica per valutare come la possibile esistenza di tale supernucleo potesse influenzare il numero di deuteroni rivelati dal rivelatore ALICE 3. Ipotesi adottate: numero di eventi generati al LHC è 10^{10} ; la temperatura di freeze-out era di 156 MeV ed il raggio di freeze-out di 8 fm con fugacità di charm di 29.6; sono state considerate solo le collisioni centrali, assunte pari al 5% del totale; si è considerato solo un gruppo ristretto di decadimenti sono stati considerati e solo i c-deuteroni con $|y| < 0.5$ si è trovato un aumento previsto di deuteroni pari a (1938 ± 12) .

Contents

1 Heavy-ion collision	7
1.0.1 Concepts of quantum chromodynamics (QCD)	7
1.0.2 The QCD phase diagram	13
1.0.3 The different stage of a heavy-ion collision	14
1.0.4 Centrality	18
2 Thermal model	19
2.0.1 Hydrodynamical description	19
2.0.2 Anisotropic flow	25
2.0.3 Statistical Hadronisation Model (SHM)	27
2.0.4 Strangeness and Charmness enhancement	30
3 $Y_c N$ bound state	33
3.0.1 One Boson exchange model	33
3.0.2 Λ_c N interaction	35
3.0.3 Possible Λ_c super-nuclei	39
3.0.4 C-deuteron ($c - d$) simulation	41
4 ALICE	51
4.1 Central barrel	54
4.1.1 Inner Tracking System (ITS)	54
4.1.2 Time Projection Chamber (TPC)	55
4.1.3 Transition Radiation Detector (TRD)	56
4.1.4 Time Of Flight (TOF)	57
4.1.5 Photon Spectrometer (PHOS)	58
4.1.6 High-Momentum Particle Identification Detector (HMPID)	58
4.1.7 Electromagnetic Calorimeter (EMCaL)	58
4.2 Forward Detectors	59
4.2.1 T0 Detectors	59
4.2.2 Zero Degree Calorimeter (ZDC)	59
4.2.3 Muon Spectrometer	60
4.3 ALICE upgrades	60
4.4 Track and vertex reconstruction	61

5 Appendix	67
A Appendix A	67
B Appendix B	68
C Appendix C	68

Chapter 1

Heavy-ion collision

1.0.1 Concepts of quantum chromodynamics (QCD)

Before talking about the dynamics of heavy-ion collision and c-deuteron production we should introduce some concepts coming from quantum chromodynamics (QCD) and the standard model (SM). The SM describes the universe at its most fundamental level and correctly predicts many results of the experiments we have ever done, sometimes with unprecedented accuracy. This theory can explain the interaction of particles with three different forces: the strong nuclear force, the weak nuclear force, and electromagnetism; while the gravity force is not yet part of the Standard Model [1]. Fortunately the absence of a quantum gravity theory, that is maybe the most fundamental lack of the SM, is not too influent in the experiment that we can actually perform. In fact physicist believe that the gravity influence will became evident only at the plank scale. This region may be characterized by particle energies of around 10^{19} GeV or 10^9 J on a single particle. The same kinetic energy of a Jumbo jet that travel at ≈ 250 km/h. However the SM is very extended and in this thesis we will only focus on the essential aspect for understanding the following chapters.

The QCD, a theory included in the SM, is the most successful theory to explain the strong interaction. The QCD assumes that strong nuclear force acts on the quarks and is mediated by gluons. The quarks are elementary particles introduced by Gell-Mann and Zweig for understand the "proliferation of the hadrons". In fact, historically, when the energy of the collision starts to increase different particles that interact with the strong force, called hadrons, were discovered. So, for explain the hundred of different hadrons detected, the two scientists proposed that this structures come form different combinations of more fundamental particles, the quarks. In particular the name quark come from the Finnegan's wake, a book of James Joyce, a writer that Gell-Mann loved. Nowadays we know six different types (flavor) of quarks usually divided in three generation. The first generations includes quark up (u) and down (d), the second the quark strange (s) and charm (c), and the last one the quark

top (t) and bottom (b).

Instead the quantum chromodynamics takes it's name because it introduces a property called color charge, the QCD analog of electric charge. First hint about the real existence of color charge was given with the discovery of Δ^{++} baryon in 1951. This baryon could only be explained imaging that it is composed of three quarks up with the spin aligned. So the configuration of the particle could be written as follows:

$$|\Delta^{++}\rangle = |u_\uparrow u_\uparrow u_\uparrow\rangle$$

a highly symmetric configuration. However, since the the particles that compose it are fermions, for the Pauli principle, they must have an overall antisymmetric wave function. In 1965, fourteen years after its discovery, this problem was finally understood by the introduction of the charge of colour. With this new parameter we can add another inner space associated to the particle and is configuration can be written as.

$$|\Delta^{++}\rangle = |u_\uparrow u_\uparrow u_\uparrow\rangle \epsilon_{ijk} [C_i \otimes C_j \otimes C_k]$$

where ϵ_{ijk} is the Ricci's tensor that permits the wave function to be anti-symmetric under quarks exchange. This is only an example but other strong supports of the color charge assumption have been discovered with the passing of time.

Quantum Chromodynamics is based on the gauge group SU(3), the Special Unitary group in 3 (complex) dimensions, whose elements are the set of unitary 3×3 matrices with determinant one. Since there are 9 linearly independent unitary complex matrices in three dimensions, the condition on the determinant reduces the set at 8 independent directions in this matrix space, corresponding to eight different generators of the group. On a physical level the presence of eight generators predicts the existence of eight different gluons. The Lagrangian density of QCD is

$$\mathcal{L} = i\bar{\psi}_q^i \gamma^\mu (D_\mu)_{ij} \psi_q^j - m_q \bar{\psi}_q^i \psi_{iq} - \frac{1}{4} F_{\mu\nu}^a F^{a\mu\nu}$$

(1.1)

where ψ_q^i denotes a quark field with colour index, γ^μ is a Dirac matrix that expresses the vector nature of the strong interaction, with μ being a Lorentz vector index, m_q , the mass of the quark, allows for the possibility of non-zero quark masses, $F_{\mu\nu}^a$ is the gluon field strength tensor for a gluon and D_μ is the covariant derivative in QCD given by $(D_\mu)_{ij} = \delta_{ij} \partial_\mu - ig_s t_{ij}^a A_\mu^a$, with g_s the strong coupling constant [2]. The coupling constant is maybe the most important parameter in defying the properties of the theory, we can imaging it as the probability that a parton, therm used for indicate both gluon and quark, of interacts in each instant of time with other partons. The possible vertices of interaction between partons are visible in Fig 1.1. Since this value is considerable during a process the higher order Feynman diagram cannot be

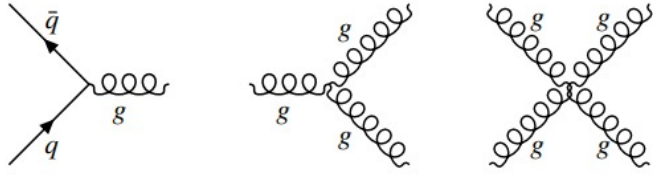


Figure 1.1: The figure show the basilar Feynman diagram of QCD.

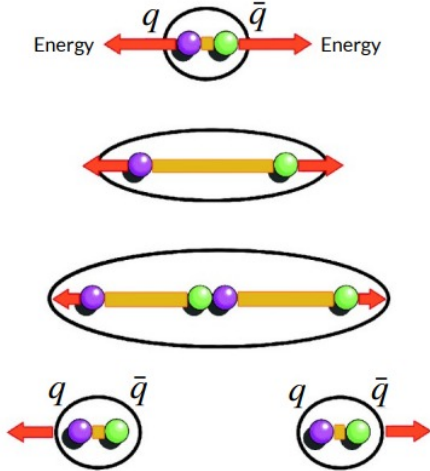


Figure 1.2: The figure resume the process of pair production of quarks. [3]

neglected therefore is particularly difficult to perform analytical calculus. So, as it is said in this cases, the theory is not perturbatively tractable. The QCD exhibits three salient properties: color confinement, asymptotic freedom and the chiral symmetry breaking.

Starting from the first one we can say that unlike one may think watching at Eq 1.1 since the gluon are massless the QCD should be a long range force. Instead the common experience tell us that only at very close distances the effect of the interaction are visible. This is possible because the energy for separate the quarks grows until a quark–antiquark pair is spontaneously produced, turning the initial hadron into a pair of hadrons instead of isolating a color charge, a graphical resume is visible in Fig 1.2. This is a very efficient way for dissipate the energy and the final result is the production of jets of hadron clearly visible in the experimental data. For these reasons, physicists believe that a direct consequence of the theory is "colour confinement", which rules out the possibility of finding a free quark. However, a formal proof has not yet been obtained and this problem has been added to the list of Millennium Prize Problems.

The asymptotic freedom is a reduction in the strength of interactions between quarks and gluons as the energy scale of those interactions increases. In fact, if the transferred momenta during a collision are low, it is not possible

to penetrate the cloud of virtual process associated to a particle. Instead, if the transferred momenta increase is possible to deeper in the virtual process cloud and so analyze in more detail the "naked particle". In this way different behaviors of the particles are observable. The asymptotic freedom is related to the fact that the quark-antiquark loop has a shielding effect of the color charge and the gluon loop has an anti screening effect. In particular, we can express the coupling constant as.

$$g_s(Q^2) = \frac{g_s(\mu^2)}{1 + g_s(\mu^2) \frac{11n_c - 2n_f}{12\pi} \ln\left(\frac{Q^2}{\mu^2}\right)} = \frac{g_s(\mu^2)}{1 + g_s(\mu^2) \frac{21}{12\pi} \ln\left(\frac{Q^2}{\mu^2}\right)} \quad (1.2)$$

where μ is a generic transferred quadri-momenta as Q , n_f is the number of known flavor (assumed six in the SM), n_c the number of color (assumed three), since $11n_c > 2n_f$ the anti-shielding effect of the gluon loop is prevalent. From the Eq 1.2 we can desume that the coupling decrease when the transferred momenta increase. The Eq 1.2 is usually expressed showing the scale factor.

$$g_s(Q^2) = \frac{1}{\frac{1}{g_s(\mu^2)} + \frac{21}{12\pi} \ln\left(\frac{Q^2}{\mu^2}\right)} \quad (1.3)$$

defining

$$\frac{1}{g_s(\mu^2)} = \frac{21}{12\pi} \ln\left(\frac{\mu^2}{\Lambda_{CQD}^2}\right) \quad (1.4)$$

$$g_s(Q^2) = \frac{1}{\frac{21}{12\pi} \ln\left(\frac{\mu^2}{\Lambda_{CQD}^2}\right) + \frac{21}{12\pi} \ln\left(\frac{Q^2}{\mu^2}\right)} = \frac{1}{\frac{21}{12\pi} \ln\left(\frac{Q^2}{\Lambda_{CQD}^2}\right)} \quad (1.5)$$

In this way is more evident the point at withc the logarithm diverges and the QCD becomes perturbatively tractable. Experimentally it is found $\Lambda_{QCD} \sim 200 \div 300$ Mev [4]. The asymptotic freedom of QCD was discovered in 1973 by David Gross and Frank Wilczek, [5]. and independently by David Politzer in the same year. For this work, all three shared the 2004 Nobel Prize in Physics. With the advent of computers, it has become possible to perform lattice QCD simulations. These simulations can be carried out in the non-perturbative condition to study the strong interaction by discretizing spacetime into a lattice, which makes it possible to calculate the behavior of quarks and gluons numerically. Before the advent of these advanced computing resources, such detailed simulations were impractical due to the immense complexity of solving the QCD equations at low energies. However, lattice QCD simulations can be very expensive and compromises are necessary.

Lastly, we can talk about the Chiral symmetry breaking. Massless fermions in Dirac theory are described by left- or right-handed spinors. The difference is related to the fact that a particle can have spin either aligned (right-handed chirality), or counter-aligned (left-handed chirality), with his momentum. In the case of massless fermion chirality is a conserved quantum number and

the left and right handed spinors can be independently phase transformed. A Dirac mass term explicitly breaks the symmetry but in QCD, the lowest mass quarks are nearly massless and it exists an approximate chiral symmetry making the system spontaneously prefer a certain configuration. In fact the vacuum in QCD is non-trivial. It is not simply empty space, but has a rich structure in which quark-antiquark pairs are constantly created and annihilated. For this reason, it is described as a superposition of many states, and the interactions between quarks and gluons cause the system to favour a particular configuration, which spontaneously breaks the chiral symmetry. The spontaneous symmetry breaking produces hadrons masses far above the one of the quarks. Yoichiro Nambu was awarded the 2008 Nobel Prize in Physics for elucidating the phenomenon in 1960. Lattice simulations have confirmed all his generic predictions [6].

For our discussion the Polyakov loop operator gets a particular importance:

$$L = \frac{1}{3} Tr \left(P e^{ig \int_0^\beta d\tau A_4(\vec{x}, \tau)} \right) \quad (1.6)$$

where P is the path-ordering operator and A_4 is the Euclidean temporal component of the gauge field and $\beta = \frac{1}{T}$ in natural unit, T temperature. A vanishing thermal expectation value $\langle L \rangle$ of the Polyakov loop operator thus indicates infinite energy for a free quark, i.e. quark confinement. It's possible to proof that as the temperature increases $\langle L \rangle$ increases rapidly to a nonzero value at high temperatures. This indicates that quark confinement is broken at the corresponding critical temperature T_{cr} . Experimentally it is found that $T_{cr} \sim 160$ MeV, which corresponds approximately to $1.86 \cdot 10^{12}$ K [7]. However, this doesn't mean that we can find free quark, because the strong force is still there and the quark can't escape by flying away.

We have already discuss that in the absence of quark masses the Eq 1.1 is chirally symmetric. Since the up and down quark masses are very small, neglecting them is a good approximation. Anyway when the temperature decreases the approximate chiral symmetry breaks generating a dynamic mass, the so called "constituent" masses. In vacuum this constituent mass are thus about 300 MeV for the up and down quarks, about 450 MeV for the strange quark, 1.5 Gev for the charm, 4.5 Gev for bottom and 180 Gev for top [4]. The dynamically generated masses disappear at T_{cr} , making the quarks light again and restoring the approximate chiral symmetry of QCD. The dissolution of massive hadrons into almost massless quarks and gluons at T_{cr} leads to a very rapid rise of the energy density near the deconfinement transition, as shown in Fig 1.3. For a massless gas of quarks and gluons the energy density is proportional to T^4 . It's possible to note that for $T < 4T_{cr}$ the data remain about 20% below this Stefan-Boltzmann limit. Instead near T_{cr} the ratio ϵ/T^4 drops rapidly by more than a factor 10. This is due to hadronization that we will discuss in the following chapters. According to Fig 1.3 the critical energy density for deconfinement is about $0.6 \div 0.7$ GeV/fm 3 . However we can have

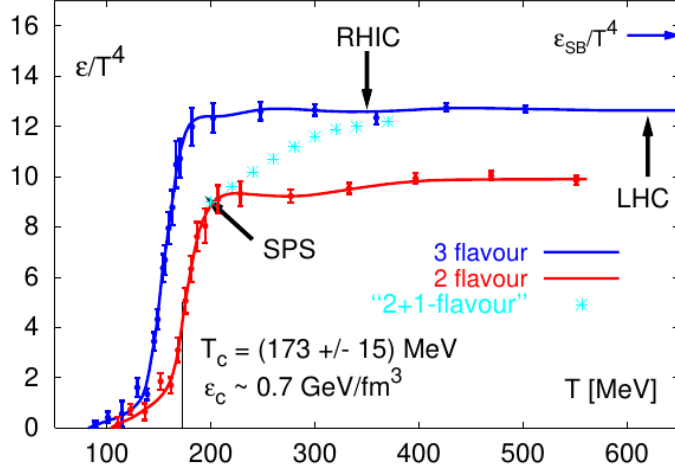


Figure 1.3: The symbol ϵ stands for energy density, the curves labelled “2 flavour” and “3 flavor” were calculated for two and three light quark flavors of mass $\frac{m_q}{T} = 0.4$. “2+1 flavour” indicates a calculation for two light and one heavier strange quark flavor of $\frac{m_q}{T} = 1$ [7].

information about the temperature and not directly on the energy density. So the uncertainty of ± 15 MeV reported in the graph on T_{cr} introduce a $\pm 40\%$ uncertainty in the critical energy density, thanks to the T^4 proportional relation, which could be as large as $1 \text{ GeV}/fm^3$ or as small as $500 \text{ MeV}/fm^3$. The dependence of T^4 is particularly important because for exceed the critical temperature by only 30% in order to reach the upper edge of the transition region, an energy density $\epsilon \approx 3.5 \text{ GeV}/fm^3$ is required and to reach $2T_{cr}$ the energy density has to arrive at $23 \text{ GeV}/fm^3$ [8]. The former number is approximately the value obtained in Pb-Pb collisions at $\sqrt{s_{NN}} = 17 \text{ GeV}$. Under the assumption that the total momentum in the region is null we can compute the energy density for colliding nuclei as

$$\langle \epsilon \rangle = 2\rho_0\gamma^2 = \frac{\sqrt{s_{NN}}^2}{2Vm c^2} \quad (1.7)$$

where ρ_0 indicates the energy density at rest of each nucleus and γ is the Lorentz factor of the beam, V the volume and m the mass. In heavy-ion collision at the Relativistic Heavy Ion Collider (RHIC) for Au-Au collision at $\sqrt{s_{NN}} = 200 \text{ GeV}$ and $R \approx 6.98 \text{ fm}$ $\langle \epsilon \rangle = 3 \cdot 10^3 \text{ GeV}/fm^3$ while for Pb-Pb collision at $\sqrt{s_{NN}} = 5.02 \text{ TeV}$ and $R \approx 7.11 \text{ fm}$ $\langle \epsilon \rangle = 2 \cdot 10^6 \text{ GeV}/fm^3$, much larger than ϵ_{cr} [9]. A more precise formulation of the energy density, valid as long as the particle production exhibits a “plateau” structure in the central rapidity region and the net baryon number at mid-rapidity is close to zero, was given by Bjorken [10]

$$\langle \epsilon_B \rangle = \frac{1}{\tau_f \pi R^2} \frac{d\langle E \rangle}{dy} \quad (1.8)$$

where τ_f stands for the formation time of the fireball and R is the transverse radius of the participant volume and πR^2 is the nuclei overlap area and y is the rapidity $y = \frac{1}{2} \ln \frac{E+p_z c}{E-p_z c}$ where z is the axis along which the beam is aligned [11].

1.0.2 The QCD phase diagram

Under extreme conditions of density and temperature, hadrons “melt” and release their contents of quarks and gluons. This is possible because at short distances and large momentum transfers, the strong interaction is not intense enough to bring the partons together and hadron structures are no longer possible. Color charges are then deconfined, and this state is called Quark-Gluon Plasma (QGP). For this reason is possible to consider QGP as the deconfined state of QCD matter and is the hottest and most dense liquid known to humankind. Furthermore, according to the most widely accepted cosmological model, the Λ CDM, were the condition of our universe only few microseconds after the Big Bang [12].

For the description of this transition the baryon chemical potential μ_B have to be introduced. It is a thermodynamic coordinate like temperature, best understood as the energy required by the system to change its chemical composition. It is tightly connected with the density of quarks: when the former is zero, the latter vanished as well, but we will discuss it better later. A simple description of the phases of nuclear matter is given in Fig. 1.4. Par-

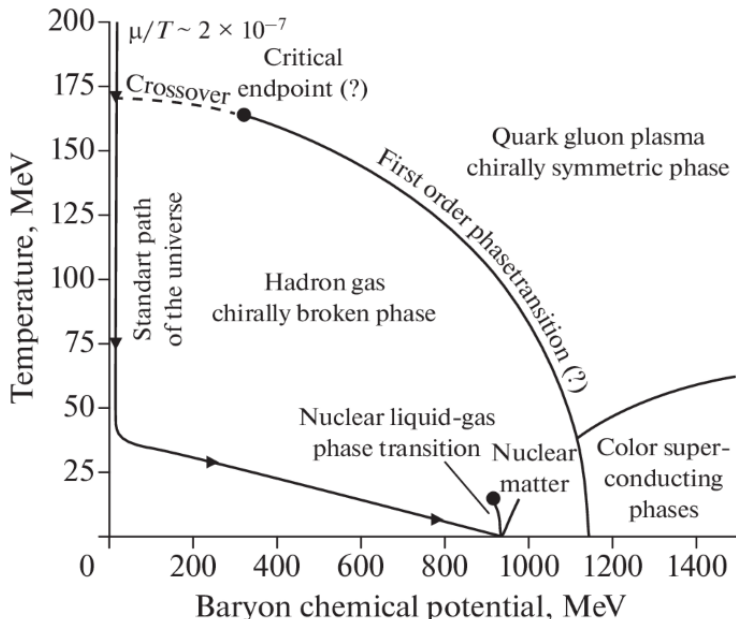


Figure 1.4: A sketched view of the phase diagram of strongly interacting matter, in the plane of temperature and the baryon chemical potential that represents the amount of net baryon charge available in the system [13]

ticularly problematic is the study of the diagram when μ_B approaches zero, like in the condition of the primordial universe. As illustrate in Fig 1.4 lattice QCD provides evidence that, even for realistically small up and down quark masses, the transition at $\mu_B = 0$ is a first order rapid crossover; although the precise value where the transition occur still remains to be determined. The short line visible in correspondence of $\mu_B = 1$ GeV indicates the nuclear liquid-gas phase transition, with a critical endpoint at a temperature of about 7.5 MeV. At higher temperatures more and more hadron resonances are excited and we have a hadron resonance gas. At low temperatures and asymptotically large baryon densities quarks are also deconfined, although not in a quark-gluon plasma state but rather in a color superconductor state. In these condition matter carries color charge without loss, analogous to the conventional superconductors that can carry electric charge without loss. The superconducting state is separated from the QGP by a first order transition at a critical temperature estimated to be of the order 30-50 MeV. It is important to note that heavy-ion collisions are not a viable method for probing the colour-superconducting phase. This is due to the fact that the process of compressing nuclear matter in such collisions results in significant entropy increase and consequent heating.

Is interesting to note that if the centre-of-mass collision energy increases, the colliding nuclei become increasingly transparent with respect to each other. Consequently a decreasing fraction of the beam energy and of the incoming baryons get stopped in the center of mass. When the energy increases the incoming net baryon number decreases, making the system more baryon-antibaryon symmetric and pushing μ_B closer to zero. At the LHC the entropy per baryon ratio S/A can reach several thousand, still far from the early universe ratio of 10^9 , that is, for all practical purposes, “baryon-free” ($\mu_B = 0$) QCD matter [8].

1.0.3 The different stage of a heavy-ion collision

The main stages of relativistic heavy-ion collisions are: collision, pre-equilibrium, thermalization, hadronization, chemical freeze-out, and decoupling. This section came from the following article [8], [7], [14], [15] and [11].

1. **Collision:** At $t=0$ the collision take place. The nuclei are highly Lorentz contracted and an extremely dense region of partons is generated with a large energy deposit in the overlap region of the collision. The superposition occur in $t_{coll} = 2 \frac{R_N}{\gamma c}$, where R_N is the nucleus radius. In Pb-Pb collision at $\sqrt{s_{NN}} = 5.02$ TeV $t_{coll} \sim 6 \cdot 10^{-3}$ fm/c, smaller than the strong-interaction timescale $t_{QCD} \sim 1$ fm/c.
2. **Pre-equilibrium** ($t < 1$ fm/c): The two nuclei just collided. The partons of the participating nucleons interact producing a large amount of

quarks and gluons. This process leads to generate high-momentum partons (the transverse momenta is $p_\perp \gg 1 \text{ GeV}/c$) creating jets or heavy quark with the emission of prompt photons. The system is now formed by a dense inhomogeneous droplet of strongly interacting QGP matter. In the very early collision stages the momentum transferred is huge and the particle production can be calculated in perturbative QCD. According to the Heisemberg uncertainty relation the production happens on a time scale $t \sim \frac{1}{\sqrt[2]{Q^2}}$, where Q is the momentum transfers. The key difference between elementary particle and nucleus-nucleus collisions is that the quanta created in the primary collisions between the incoming nucleons can't right away escape into the surrounding vacuum.

In a central collision between two Pb or Au nuclei the nuclear reaction zone has a transverse diameter of about 12 fm, so a hard particle created near the edge and moving towards the center (straight inward) needs about 20 fm/c before it emerges on the other side. During this time the matter thermalizes, expands, cools down and almost reaches decoupling. As the particle moves through the plasma, it loses energy. It can be shown that the energy loss is proportional to the density of the medium times the scattering cross section between the probe and the medium constituents integrated along the trajectory of the probe. In this way, important information about the medium can be analysed. Other probes of the early collision stage are direct photons, either real or virtual, and other process connected to QED such the creation of a couple lepton-antilepton generally known as “dileptons”. In contrast to all hadronic probes, they thus escape from the collision zone without reinteraction and carry pristine information about the momentum distributions of the particle that generated them. Anyway the directly emitted photons and dileptons must be must be searched in a chaotic background of indirect photons and particle generated in other process. This makes the measurement of these signals particularly difficult.

3. **Thermalization** ($t \sim 1 - 15 \text{ fm}/c$): The constituents of the fireball interact frequently, establishing a local equilibrium state. This phase is characterised by a thermally equilibrated nature, which makes the QGP exhibit perfect fluid behaviour and allows a hydrodynamic description of the medium. This refers to its exceptionally low viscosity, minimal internal friction and high thermal conductivity. Experimental observations, in particular those related to the collective flow of particles produced in heavy-ion collisions, support this behaviour. The partons produced rescatter both elastically and inelastically. Both types of collision lead to an equipartition of the deposited energy, but only the inelastic ones change the chemical composition of the medium by changing the flavour of the partons. The system, now in equilibrium, builds up an internal pressure that is unopposed by the surrounding void. This leads to a

rapid hydrodynamic expansion of the system with a decrease in temperature and energy density.

4. **Hadronization** ($t \sim 20$ fm/c) As the temperature lowers, the energy density of the system is no longer able to keep the partons apart, and hadrons begin to form as the energy density approaches ϵ_{cr} . During this phase the entropy density drops because of the recombination. However this parameter cannot decrease. This implies that the fireball volume must increase by a large factor while the temperature remains approximately constant. Since the growth of the fireball volume takes time the systems spend significant time near T_{cr} . While the matter hadronizes it's speed of sound $v_s = \sqrt{\frac{\partial p}{\partial e}}$ is small causing inefficient acceleration that doesn't permit the collective flow increase during this phase.
5. **Chemical freeze-out:** When the temperature decreases enough inelastic interactions among hadrons are completely stopped and only the elastic one occur. This happen because at this point the matter becomes so dilute that the average distance between hadrons exceeds the range of the strong interactions. The hadrons abundance "freeze out" but the creation of some resonance is still possible but such processes does not change the finally observed chemical composition. Since most of the hadrons in a relativistic fireball are pions, very light particle $m_\pi \sim 140$ MeV, resonances with them are very efficient in keeping the system in thermal equilibrium. The chemical freeze-out occur when $T = T_{ch}$.
6. **Kinetic freeze-out:** At this stage the hadrons, including the unstable resonances, start to decouple from the medium as the temperature lowers and the mean free path becomes larger than the mean distance between hadrons. This mean that particles are no longer subject to significant interactions and can travel freely to the detector. The distribution of kinetic energy among all hadrons has now ceased and the transverse momentum spectrum is approximately exponential while the unstable resonances decay in particle with smaller transverse momenta. Given that the majority of resonances decay by emitting pions, this effect is of particular importance for their spectra, which at low transverse momenta are dominated by decay products. The kinetic freeze-out occur when $T = T_{kin} \sim 153$ MeV.

A graphical resume of the process is visible in Fig 1.5 and 1.6.

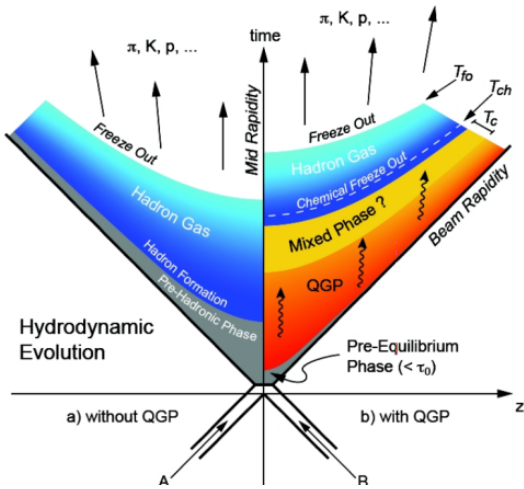


Figure 1.5: Evolution of a central heavy-ion collision in a Minkowski-like plane. The two scenarios with and without QGP are pointed out. The critical temperature is indicated by T_c , while the freeze-out and chemical freeze-out temperatures, are pointed out with T_{fo} , and T_{ch} , respectively [16].

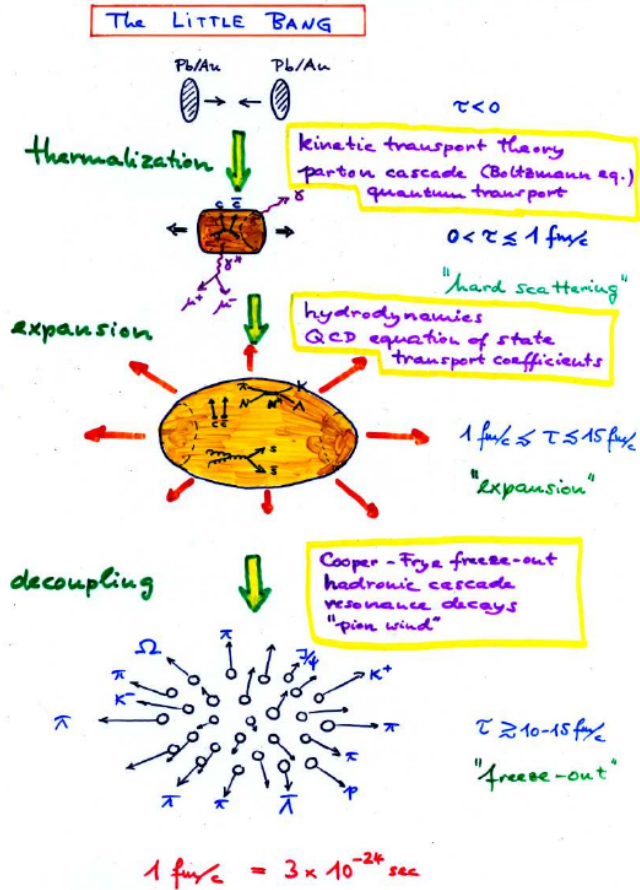


Figure 1.6: A sketched view of the phase of the system after the collision [8].

1.0.4 Centrality

An important parameter to characterize heavy-ion collisions is the centrality, an observable related to the transverse distance (\vec{b}) between the centers of the colliding nuclei. Interactions with the smallest $|\vec{b}|$ are called central collisions, while those with large $|\vec{b}|$ are called peripheral collisions. This parameter is expressed in terms of the fraction of the total cross section σ_{AA} . The centrality percentile of collisions with impact parameters in the interval $[b_1, b_2]$ is given by

$$c(b_1, b_2) = \frac{\int_{b_1}^{b_2} db \frac{d\sigma}{db}}{\int_0^\infty db \frac{d\sigma}{db}} = \frac{\int_{b_1}^{b_2} db \frac{d\sigma}{db}}{\sigma_{AA}} \quad (1.9)$$

Centrality has important consequences for the expected particle abundances, in particular the number of charged particles. The total number of charged particles produced in a collision is a commonly used observable called the multiplicity. For this reason, the centrality can be obtained experimentally from the measure of the multiplicity or by counting the number of spectator nucleons, the nucleons that do not interact during the collision. The centrality of each collision must be determined experimentally in order to identify peculiar behaviour that can occur for very specific centrality classes. It is interesting to report that only 5% of the total cross section corresponds to a central interaction [11]. The centrality can be used to calculate the number of interacting (participant) nucleons $N_{part}(b)$ and the total number of binary nucleon-nucleon collisions $N_{coll}(b)$. The Glauber model formulation [17] assumes that: the nucleons are point-like and independent, their trajectory is a straight line, the nucleon-nucleon inelastic cross section does not vary during the collision, hypotheses known as optical limit. If we call A and B the number of nucleons in the first and second nucleus respectively, the probability of nucleon-nucleon interactions is given by the binomial distribution.

$$p(n, \vec{b}) = \binom{AB}{n} \left[T_{AB}(\vec{b}) \sigma_{inel}^{NN} \right]^n \left[1 - T_{AB}(\vec{b}) \sigma_{inel}^{NN} \right]^{AB-n} \quad (1.10)$$

Where σ_{NN} is the cross section and T_{AB} is the nuclear overlapping function, it can be computed from the single nucleon distribution of the interacting nuclei. It's possible to imagine this parameter as probability to have a nucleon at the same position in the transverse plane in both colliding nuclei. From the mean value of the binomial,

$$\langle N_{coll}(b) \rangle = A B T_{AB}(\vec{b}) \sigma_{inel}^{NN} \quad (1.11)$$

So the number of participant is given by:

$$\begin{aligned} \langle N_{part}(\vec{b}) \rangle &= A \int d^2 s T_A(\vec{s}) \left[1 - \left(1 - T_B(\vec{b} - \vec{s}) \sigma_{inel}^{NN} \right)^B \right] \\ &\quad + B \int d^2 s T_B(\vec{b} - \vec{s}) \left[1 - \left(1 - T_A(\vec{s}) \sigma_{inel}^{NN} \right)^A \right] \end{aligned} \quad (1.12)$$

with T the thickness function [15].

Chapter 2

Thermal model

2.0.1 Hydrodynamical description

This section resume the information of [8], [18].

We have already seen that the fireball can be approximately described as an ideal fluid. This approximation holds if the microscopic scattering time scale is much shorter than any macroscopic time scale associated with the fireball evolution. So hydrodynamics becomes applicable when the mean free path of the particles is much smaller than the system size. For these reason the fact that the QGP behaves like an ideal fluid implies strong non-perturbative interactions in the quark-gluon plasma phase. Hydrodynamics allows a description of the system in terms of macroscopic quantities so an equation that connect the pressure, the energy density and baryon density i.e. an equation of state is required. Lattice QCD suggests a simplified equation of state for an ideal massless gas:

$$P_{pressure} = \frac{\epsilon}{3} = \frac{d\pi^2 T^4}{90} \quad (2.1)$$

where d is the effective number of degrees of freedom, value of $d = 47.5$ for a three flavor QGP which is an order of magnitude larger than that of a pion gas where $d \sim 3$ [19].

The possibility to describe the evolution of the fireball in terms of macroscopic quantities makes hydrodynamics the ideal language, as it allows the description of the hadronisation phase transition without the need for a microscopic description, and at the same time explains the observed collective flow phenomena.

The particles velocities in the fireball are under the effect of pressure gradients and are not independent. For this reason in the final state particle velocities will not be distributed according to random thermal motion, but instead will keep a collective ones. This means that, as happen in an expanding gas, the momentum distribution of particles depend on the position in the plasma and is not completely randomical. This feature is commonly called “collective flow” as opposed to the “non-collective flow” in which particles show uncorrelated velocities. To define the collective flow we can consider

any space-time point in the fireball and consider an infinitesimal volume associate with the point. So the flow velocity can be expressed by $\vec{v}(x) = \frac{|\vec{P}|}{P^0}$, where \vec{P} is the mean 3-momentum of the particle in the volume and P^0 is the mean energy in quadrivectorial formalism. It's possible to associate at $\vec{v}(x)$ a normalized velocity $u^\mu = \gamma(1, \vec{v}(x))$ where γ is the Lorentz factor. In the same manner we can define $T(x)$ the average local temperature and the μ_i , the chemical potential of the i-th particle species. It's possible to separate the flow velocity into its components along the beam direction (“longitudinal flow” $\vec{v}_l(x)$) and in the plane perpendicular to the beam (“transverse flow” $\vec{v}_\perp(x)$). From now on the natural unit will be used. In this case the phase-space distribution of particles of type i is given by the Lorentz covariant local equilibrium distribution:

$$f_{i,eq}(x, p) = \frac{g_i}{e^{(p \cdot u - \mu_i)/T} + \theta_i} = g_i \sum_{n=1}^{\infty} (\theta_i)^n e^{n(p \cdot u - \mu_i)/T} \quad (2.2)$$

Here g_i is a spin-isospin-color-flavor-etc. degeneracy factor which counts all particles with the same properties. The factor $p \cdot u$ ¹ is the energy of the particle in the local rest frame. The θ_i in the denominator accounts for the proper quantum statistics of particle (+1 for fermions and -1 for bosons). The Boltzmann approximation corresponds to keeping only the first term in the sum in the last expression. In our applications this is an excellent analytical approximation for all hadrons except for the pion because of their mass.

At relativistic energies it is convenient to parametrize the longitudinal flow velocities and momenta in terms of rapidities and pseudo-rapidities, $\eta = \frac{1}{2} \ln \frac{1+v}{1-v}$ in this way $v = \tanh(\eta)$. It's also possible to define $\eta_l = \frac{1}{2} \ln \frac{1+v_l}{1-v_l}$ and $y = \frac{1}{2} \ln \frac{1+\frac{p_l}{E}}{1-\frac{p_l}{E}} = \frac{1}{2} \ln \frac{E+p_l}{E-p_l}$. Rapidities have the advantage over longitudinal velocities that they are additive under longitudinal boosts. In fact it is possible to express η'_l in a given inertial frame which moves relative to the first frame with rapidity $\Delta\eta$ in the -z direction as $\eta'_l = \eta_l + \Delta\eta$. In addition the previous expression simplified:

$$u^\mu = \gamma_\perp (\cosh \eta_l, v_x, v_y, \sinh \eta_l) \quad (2.3)$$

$$p^\mu = (m_\perp \cosh y, v_x, v_y, m_\perp \sinh y) \quad (2.4)$$

Where $\gamma_\perp = \frac{1}{\sqrt{1-v_\perp^2}}$ and $m_\perp = \sqrt{m^2 + p_\perp^2}$ is the transverse mass. For convenience we define also $\tau = \sqrt{t^2 - z^2}$, the longitudinal proper time and z the longitudinal position, and $\vec{r}_\perp = (x, y)$.

¹this expression correspond to the quadrivectorial scalar product with the metrical tensor $P^\mu u_\mu = g_{\mu\nu} P^\mu u^\mu$

$$g_{\mu\nu} = \begin{pmatrix} 1 & 0 & 0 & 0 \\ 0 & -1 & 0 & 0 \\ 0 & 0 & -1 & 0 \\ 0 & 0 & 0 & -1 \end{pmatrix}$$

Bjorken argued that at asymptotically high energies the physics of secondary particle production should be independent of the longitudinal reference frame. Furthermore, the boost-invariance of these initial conditions is preserved in longitudinal proper time if the system expands collectively along the longitudinal direction, in this approximation hold $\eta = \eta_l$. For more details see [10]. The Bjorken scaling approximation is expected to be good at high energies and not too close to the beam and target rapidities. We can so said that

$$p \cdot u(x) = \gamma_\perp(\vec{r}_\perp, \tau) (m_\perp \cosh(y - \eta) - \vec{p}_\perp \cdot \vec{v}_\perp(\vec{r}_\perp, \tau)) \quad (2.5)$$

The Cooper-Frye formula

In this section we will discuss a formalism for count the total number of particles of species i produced in the collision. Since this value does not depend on the reference frame of the observer, we must be able to express it in a Lorentz-invariant way. We define a three-dimensional hypersurface $\Sigma(x)$ in 4-dimensional space-time along which we perform the counting. It's clear that different choices for the hypersurface are possible and the final result must not change as long as it completely closes off the future light cone emerging from the collision point. So for obtaining the count of total particles of each species produced we can study how many particles cross the surface. A possible way for obtain the desired result consists in subdividing the hypersurface into infinitesimal elements $d^3\sigma$ and then summing on them. Defining an outward-pointing 4-vector $d^3\sigma_\mu(x)$ perpendicular to $\Sigma(x)$ at point x with the magnitude $d^3\sigma$. Introducing the 4-vector j_i^μ describing the current of particles i through point x , and summing over all the infinitesimal hypersurface elements we get

$$N_i = \int_{\Sigma} d^3\sigma_\mu(x) j_i^\mu(x) = \int_{\Sigma} d^3\sigma_\mu(x) \left(\frac{1}{(2\pi)^3} \int \frac{d^3p}{E} p^\mu f_i(x, p) \right) \quad (2.6)$$

Where $j_i^\mu(x)$ is the particle number current density given in terms of the Lorentz-invariant phase-space distribution. The normal vector can be computed assuming longitudinal boost-invariance, the freeze-out surface can be characterized by a longitudinal proper time. It's possible to proof that

$$d^3\sigma_\mu = \left(\cosh \eta, -\frac{\partial \tau_f}{\partial x}, -\frac{\partial \tau_f}{\partial y}, \sinh \eta \right) \tau_f d^2 r_\perp d\eta \quad (2.7)$$

If the freeze-out surface is $\Sigma_f = (t_f, x_f, y_f, z_f) = (\tau_f \cosh \eta, \vec{r}_\perp, \tau_f \sin \eta)$, by multiplying the latter parameters with the velocity $\frac{p^\mu}{E}$ and integrating over all momenta with measure $\frac{d^3p}{(2\pi)^3} = \frac{d^3p}{(2\pi)^3}$, we finally obtain the Cooper-Frye

formula

$$\boxed{E \frac{dN_i}{d^3p} = \frac{dN_i}{dyp_\perp dp_\perp d\phi_p} = \frac{dN_i}{dym_\perp dm_\perp d\phi_p} = \frac{1}{(2\pi)^3} \int_{\Sigma} p \cdot d^3\sigma_{\mu}(x) f_i(x, p)} \quad (2.8)$$

Where ϕ_p is the azimuthal angle. Combing the Eq. 2.7 and 2.5 one gets:

$$p \cdot d^3\sigma_{\mu} = (m_\perp \cosh(y - \eta) - \vec{p}_\perp \cdot \nabla_\perp \tau_f(\vec{r}_\perp)) \tau_f d^2r_\perp d\eta \quad (2.9)$$

To compute the measured momentum spectrum we can therefore replace the surface Σ by shrinking it to the smallest and earliest surface that still encloses all the processes. It is called the “surface of last scattering” or “freeze-out surface” Σ_f . The the number of particles obtained from the Cooper-Frye formula is not always positive-definite. Physically negative contributions of the Cooper-Frye formula correspond to particles that stream backwards into the hydrodynamical region. It’s possible to compare the negative contribution with the total number particles crossing the transition hypersurface. It is found that the number of underlying inward crossings is much smaller than the one the Cooper-Frye formula gives under the assumption of equilibrium distribution functions [20].

To compute the measured momentum spectrum the knowledge of the phase-space distribution on the surface of last scattering is required. Since the transition from strong coupling to free-steaming thus happens in a short time interval we may approximate $f_i(x, p)$ on the last scattering surface. In this section we report only the final momentum distribution obtainable from the Eq. 2.8 result but the proof is in the appendix A.

$$\begin{aligned} \frac{dN_i}{dym_\perp dm_\perp d\phi_p} &= \frac{g_i}{\pi} \int_0^\infty r_\perp dr_\perp n_i(r_\perp) \left[m_\perp K_1 \left(\frac{m_\perp \cosh(\rho(r_\perp))}{T(r_\perp)} \right) \right. \\ &\quad I_0 \left(\frac{p_\perp \sinh(\rho(r_\perp))}{T(r_\perp)} \right) - p_\perp \frac{\partial \tau_f}{\partial r_\perp} K_0 \left(\frac{m_\perp \cosh(\rho(r_\perp))}{T(r_\perp)} \right) \\ &\quad \left. I_1 \left(\frac{p_\perp \sinh(\rho(r_\perp))}{T(r_\perp)} \right) \right] \end{aligned} \quad (2.10)$$

That includes the modified Bessel functions and $v_\perp = \tanh \rho$. This formula is useful because it allows to easily perform systematic studies of the influence of the radial profiles of temperature, density and transverse flow on the transverse momentum spectrum, in order to better understand which features of a real dynamical calculation of these profiles control the shape of the observed spectra.

Eq. 2.10 can be simplified by assuming instantaneous freeze-out. In this case there is no dependence of the proper time at the freeze-out surface τ therefore $\frac{\partial \tau}{\partial r_\perp} = 0$ so we can rewrite the previous equation in the following manner:

$$\frac{dN_i}{dy m_\perp dm_\perp} = \frac{g_i}{\pi^2} \int_0^\infty r_\perp dr_\perp n_i(r_\perp) \left[m_\perp K_1 \left(\frac{m_\perp \cosh(\rho(r_\perp))}{T(r_\perp)} \right) I_0 \left(\frac{p_\perp \sinh(\rho(r_\perp))}{T(r_\perp)} \right) \right] \quad (2.11)$$

Commonly named Boltzmann-Gibbs blast wave. This formulation is particularly used to extract properties of the common source such as the temperature T_f or to fit the single particle spectra. The agreement of Eq. 2.11 with the spectra is quite remarkable especially in central events where the thermal description is expected to work better. However for a more precise description some models take into account also the final state interaction effects, such as the Coulomb repulsion/attraction between charged hadrons which continues long after their strong interactions with each other have ceased.

Transverse momentum spectra and freeze-out temperature

For all hadrons it is observed that $m_\perp/T > 1$ so the modified Bessel function can be approximated in the following manner $K_\nu \sim e^{-\frac{m_\perp \cosh \rho}{T}}$. At $r_\perp = 0$ the radial flow velocity must vanish by symmetry but to larger r_\perp typically it rises linearly, it eventually reaches a maximum value and drops again to zero since the dilute tail of the initial density distribution freezes out early. Some simulated profile of grow are shown in the Fig. 2.1 [21].

Different processes can manifest, for example at SPS energies the freeze-out surface moves from the edge inward since the fireball matter cools and freezes out faster than the developing radial flow can push it out. At LHC energies the much stronger radial flow generated by the much higher internal pressure makes the fireball grow considerably arriving at radius of 13 fm/c. To understand how radial flow influences the spectra, first consider the case with no flow ($\rho = 0$). in this condition $I_q(0) = 0$ and thus Eq 2.10 reduces to

$$\frac{dN_i}{dy m_\perp dm_\perp} \sim m_\perp K_1 \left(\frac{m_\perp}{T} \right) \sim m_\perp^{1/2} e^{-\frac{m_\perp}{T}} \quad (2.12)$$

In this condition as the temperature is the same for all hadrons the spectra depend only on the transverse mass, a fact known as " m_\perp " scaling. As visible in the equation the temperature can be extracted easily. Instead if the radial flow is not vanishing approximating $p_\perp \approx m_\perp$ one gets:

$$\frac{dN_i}{dy m_\perp dm_\perp} \sim e^{-\frac{m_\perp (\cosh \rho - \sinh \rho)}{T}} = e^{-\frac{m_\perp}{T_{slope}}} \quad (2.13)$$

With $T_{slope} = T \sqrt{\frac{1+v_\perp}{1-v_\perp}}$. Convective flow breaks m_\perp scaling especially at low m_\perp as in Fig. 2.2. In fact for sufficiently large hadron mass and flow velocity

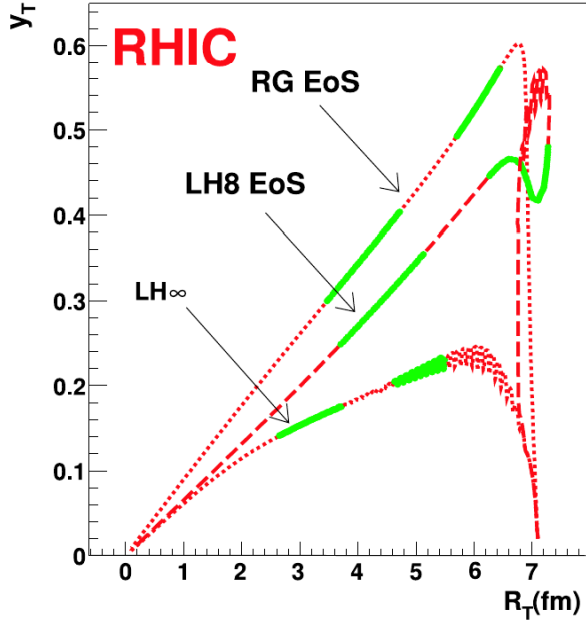


Figure 2.1: Radial flow rapidity profile $\rho(r_\perp) = y_T$ for central Au+Au collisions at RHIC, from hydrodynamic calculations employing three different equations of state [16].

the spectrum develops a blast wave peak at nonzero transverse momentum. In conclusion is possible to summarize these two important limits

$$\text{Non relativistic: } p_\perp \ll m_i \quad T_{i,\text{slope}} \approx T_f + \frac{1}{2}m_i\langle v_\perp \rangle^2 \quad (2.14)$$

$$\text{Relativistic: } p_\perp \gg m_i \quad T_{\text{slope}} = T \sqrt{\frac{1+v_\perp}{1-v_\perp}} \quad (2.15)$$

This effect is visible in Fig. 2.2 for two flow velocities. These formulations have of course their practical limitations in the fact that pions, the lightest hadrons, are quickly falling into the relativistic case and few measures were performed at low momenta, especially in collider experiments. In addition, non-relativistic pions are affected by both Bose-Einstein statistics and contribution from resonance decays. Furthermore the m_\perp -scaling is expected to be more evident for the pp collision while for the heavy-ion case the presence of the radial flow breaks the m_\perp -scaling. The modification of the spectral shape affects also the mean of the distribution in a mass-dependent way, resulting in an increase of the p_\perp with the particle mass. This increasing is expected to be more evident when flow is stronger.

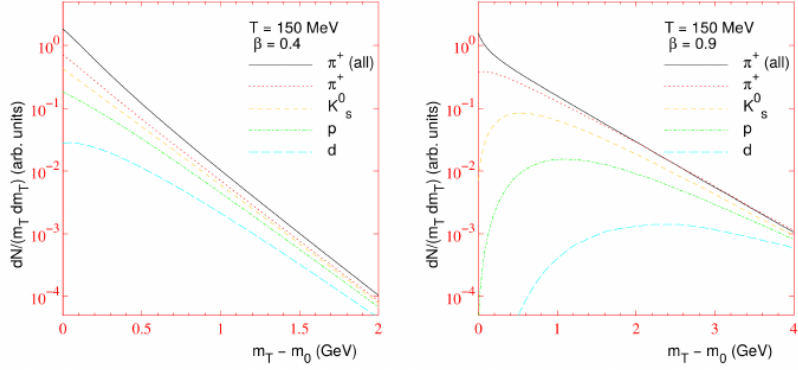


Figure 2.2: Flow spectra for various hadrons as a function of $m_{\perp} - m_0$ where m_0 is their rest mass. The calculation assumes an infinitesimally thin shell of temperature $T = 150$ MeV expanding with $\beta = 0.9$ on the right and $\beta = 0.4$ on the left. The curve labelled "π⁺ (all)" includes pions from resonance decays in addition to the thermally emitted pions.

2.0.2 Anisotropic flow

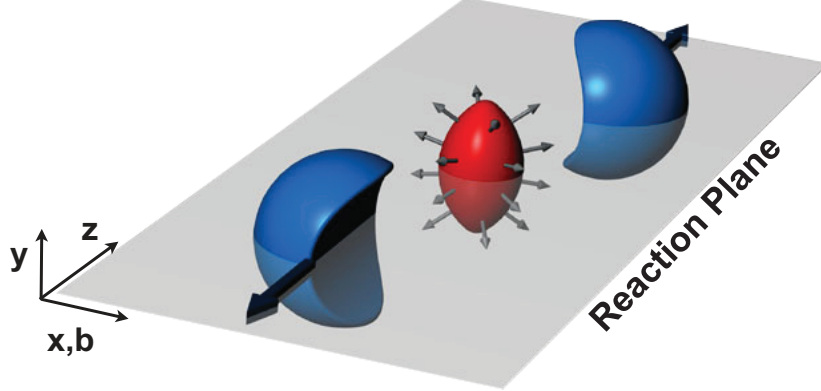


Figure 2.3: Almond shaped interaction volume after a non-central collision of two nuclei. The spatial anisotropy with respect to the x-z plane (reaction plane) translates into a momentum anisotropy of the produced particles (anisotropic flow).

This section come from [19], [8] and [22]. For central collisions between equal spherical nuclei, radial flow is the only possible type of transverse flow allowed by symmetry. In non-central collisions, however, this azimuthal symmetry is broken, and anisotropic transverse flow patterns can develop. Experimentally, anisotropic flow provides the most direct evidence of flow in the QGP, producing anisotropy in particle momentum distributions. The evolution of the elliptic shaped interaction volume is shown in Fig. 2.4 [23]. The contours indicate the energy density profile and the sequence shows the time evolution from an almost elliptical region into an almost symmetric system,

an expansion that happen at the speed of sound. In this situation the equa-

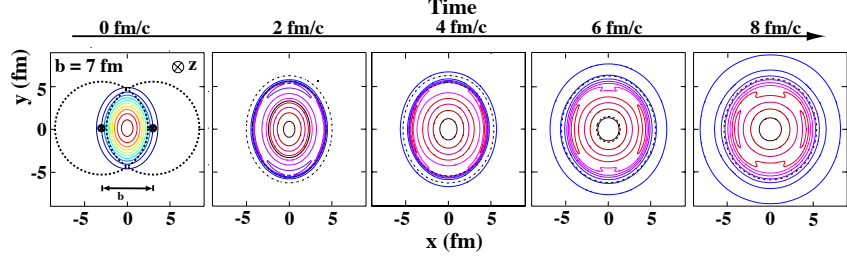


Figure 2.4: The created initial transverse energy density profile and its time dependence in coordinate space for a non-central heavy-ion collision. The z-axis is along the colliding beams, the x-axis is defined by the impact parameter.

tion 2.8 can be written using a Fourier expansion introducing b , the impact parameter modulus, and ψ_n the azimuthal angle, in the form

$$\begin{aligned} E \frac{dN_i}{d^3p}(b) &= \frac{dN_i}{dyp_\perp dp_\perp d\phi_p}(b) \\ &= \frac{1}{2\pi} \frac{dN_i}{dyp_\perp dp_\perp}(b) \left(1 + 2 \sum_{n=1}^{\infty} v_n^i(p_\perp, b) \cos(n(\phi_p - \psi_n)) \right) \end{aligned} \quad (2.16)$$

In this Fourier decomposition, the coefficients v_1 , v_2 and v_3 are known as directed, elliptic and triangular flow respectively. As visible in Fig. 2.3 the momentum space distribution has a preferred direction and this asymmetry can be quantified by the spatial ellipticity:

$$\epsilon_x(b) = \frac{\langle y^2 - x^2 \rangle}{\langle y^2 + x^2 \rangle} \quad (2.17)$$

As a function of time, ϵ_x decreases spontaneously due to free-streaming radial expansion, in the absence of rescattering, or faster when elliptic flow develops as a result of rescattering. The first mechanism is a consequence of the Heisenberg uncertainty principle: as the spatial localization improves, the uncertainty in the corresponding momentum component increases. Instead the elliptic flow is a consequence of the fact that there is high pressure in the interior of the reaction zone which falls off to zero outside. The pressure gradient is very steep in the short direction leading a stronger hydrodynamic acceleration. It's possible to show that the spatial eccentricity decrease as a function of time in the following manner, as detailed in the appendix B:

$$\frac{\epsilon_x(\tau_0 + \Delta\tau)}{\epsilon_x(\tau_0)} = \left[1 + \frac{(c\Delta\tau)^2}{\langle r^2 \rangle_{\tau_0}} \right]^{-1} \quad (2.18)$$

where τ_0 is the time when the particles were created and $\langle r^2 \rangle_{\tau_0}$ is the azimuthally averaged initial transverse radius squared of the reaction zone. Hydrodynamics predicts that heavier particles gain more momentum than lighter

ones for the previously discussed flattening of their spectra at low transverse kinetic energies. It is also known from microscopic kinetic studies that for a given initial spatial eccentricity the magnitude of the generated elliptic flow is a monotonic function of the mean free path.

More recently, it was realized that small deviations from ideal hydrodynamics, in particular viscous corrections, modify significantly the buildup of the elliptic flow. The shear viscosity determines how good a fluid is, however, for relativistic fluids the more useful quantity is the shear viscosity over entropy ratio η_v/s . For perfect fluids the ratio can be approximated by:

$$\frac{\eta_v}{s} \approx \frac{\hbar}{4\pi k_B} \quad (2.19)$$

It is argued that the transition from hadrons to quarks and gluons occurs in the vicinity of the minimum in η_v/s , just as in the phase transitions of common life substances such as water.

2.0.3 Statistical Hadronisation Model (SHM)

This section had been inspired by the folowing article [24], [25], [8] and [11].

The idea of applying statistical concepts to the problem of multi-particle production in high energy collisions dates back to a work of Fermi in 1950, who assumed that particles originated from an excited region evenly occupying all available phase space states. Note that such a statistical approach has, of course, its limitations. In fact in this way it is impossible to investigate correlations between pairs, triplets, quadruplets etc. of particles because they belong to the same event and so are not produced entirely independently but correlated in a non-statistical way. For example the momenta of the particles emerged from the fireball must conserve the original one of the initially colliding nuclei generating non-statistical correlations. So for describe this complex dynamical process, the Statistical Hadronisation Model (SHM) postulates that hadrons are formed from the decay of each cluster in a purely statistical way so. *Every multihadronic state localized within the cluster and compatible with conservation laws is equally likely.*

Often the mathematical formalism used to describe the system is the grand-canonical one, which takes into account the possibility for the volume under study to exchange both particles and energy with its surroundings. This approach is justified by the fact that in heavy-ion collisions the volume of the fireball is considerably larger than the partonic scale; indeed, the volume of clusters is in constant ratio to their mass when hadronisation takes place. For smaller systems, like happen for example in collision between protons or proton and other nucleus, the grand-canonical ensemble is no longer a good description of the system. In this case the volume created after the collision is considerably smaller and it is better to require the local conservation of quantum numbers and so the canonical formulation is more appropriate. It

is worth noting that the transition from a canonical to a grand-canonical description effectively occurs when the cluster volume is of the order of 100 fm^3 at an energy density of 0.5 GeV/fm^3 [26]. In addition one has to consider the quantum behaviour of both fermionic and bosonic degrees of freedom that form the system. Some possible effect are for example the Bose-Einstein correlations or Hanbury Brown-Twiss interference. The Bose-Einstein correlations refer to a quantum mechanical phenomenon that arises due to the wave-like nature of bosonic particles and their tendency to occupy the same quantum state. Instead the Hanbury Brown and Twiss effect is any of a variety of correlation and anti-correlation effects in the intensities received by two detectors from a beam of particles and depends on the fermionic or bosonic nature of the beam. From statistical mechanics is known that hold

$$\langle N \rangle = \frac{1}{\beta} \left(\frac{\partial \ln Z}{\partial \mu_B} \right) \quad (2.20)$$

$$\langle E \rangle = - \left(\frac{\partial \ln Z}{\partial \beta} \right) + \mu_B \langle N \rangle \quad (2.21)$$

$$\langle S \rangle = k_B \frac{\partial T \cdot \ln Z}{\partial T} \quad (2.22)$$

$$P_{pressure} = \frac{1}{\beta} \left(\frac{\partial \ln Z}{\partial V} \right) \quad (2.23)$$

Where $E, S, P_{pressure}, N, T$ and k_B are respectively the energy, the entropy, the pressure, the number of particle, the temperature and the Boltzmann constant, instead $\beta = \frac{1}{k_B T}$ and Z is the partition function that can be expressed in the following manner

$$\boxed{\ln Z_i(T, V, \mu_i) = \frac{\Delta V g_i}{2\pi^2 \hbar^3} \int_0^\infty \theta_i p^2 dp \ln (1 + \theta_i e^{\beta(\mu_i - E)})} \quad (2.24)$$

θ_i , already defined, is +1 for fermions and -1 for bosons, and g_i is the overall degeneracy. Global observables such as the particle mean multiplicities and entropy can be derived from the previous equation:

$$\boxed{\langle N \rangle = \frac{\Delta V g_i}{2\pi^2 \hbar^3} \int_0^\infty dp \frac{p^2}{e^{-\beta(\mu_i - E)} + \theta_i}} \quad (2.25)$$

$$\langle S \rangle = - \sum_i \int_{\Delta V} \int \frac{d^3x d^3p}{(2\pi)^3} [f_i \ln f_i + \theta_i (1 - \theta_i f_i) \ln (1 - \theta_i f_i)] \quad (2.26)$$

In this case the distribution is a bit different from Eq. 2.2.

$$f_{i,eq}(x, p) = \frac{g_i}{e^{\beta(\Delta V)(E_i - \mu_i(\Delta V))} + \theta_i} \quad (2.27)$$

The Eq. 2.24 can be further developed by considering Taylor expansion of the logarithmic part, the full derivation is given in the appendix C.

$$\ln Z_i(T, V, \mu_i) = \frac{\Delta V g_i}{2\pi^2 \hbar^3 \beta} \sum_K \frac{(\theta_i e^{\beta \mu_i})^k}{k^2} m_i^2 K_2(k\beta m_i) \quad (2.28)$$

The definition of the chemical potential μ_i is strictly related to the processes under study and to the type of chosen ensemble formalism. It became necessary in order to take into account the possibility to have fluctuations in the number of particles of species i. For a given species i the chemical potential can be split into $\mu_i = B_i \mu_B + S_i \mu_S + Q_i \mu_Q$, where B_i , S_i and Q_i are respectively the baryon number, strangeness and electric charge while μ_B , μ_S and μ_Q are the corresponding chemical potentials. If the energy of the collision is not enough the strange quark and antiquark can be non thermalized. So we should add another term to chemical potential. This term take the form $|s_i| \bar{\mu}_s$ where s_i is the total number of strange quarks and antiquarks in hadron and $\bar{\mu}_s$ the corresponding potential. In heavy-ion collisions, however, the s quarks can be fully thermalised. Similarly to the strange quark, the same process can be repeated for the heavier flavours.

Starting from measurements of the identified particle yields (dN/dy) in the light flavor sector by using the SHM approach one gains access to the thermodynamic properties of the system created in the collision. An example of such measurement for different particle species is given in Fig. 2.5. It is possible to identify some key features:

- Particles and antiparticles tend to be equally produced if the collision energy is high enough. This is especially true at LHC energies.
- Baryons and mesons follow different behaviour with significant baryon/anti-baryon discrepancies at lower energies.
- Pions are the most abundant particle species produced
- Particles containing s or c quarks are subject to a significant increase in their abundances at opportune energy. This effect known as “strangeness enhancement” was historically identified as a typical signature of the QGP. This aspect will be discussed better later.
- At high energies the production of particles with same mass but different quark content tends to be similar.

The SHM can be used to fit the measured dN/dy using only a limited number of parameters. This allows to obtain quantities such as the chemical freeze-out temperature, the system volume V and the chemical potential μ_B . Fig. 2.6 shows how the best fit parameters to describe the data from Pb–Pb central collisions collected by the ALICE experiment at $\sqrt{s_{NN}} = 2.76$ TeV are: $T = 156.5 \pm 1.5$ MeV, $\mu_B = 0.7 \pm 3.8$ MeV, $V = 5280 \pm 410$ fm³.

The model is able to describe reasonably well measurements of yields which span over 9 order of magnitudes with a $\tilde{\chi}^2 = 1.61$ with a low number of free parameters [27]. In addition these results allow for a direct comparison with predictions from lattice QCD. Such comparison is resumed in Fig. 2.7 where is possible to see that the curve is correctly described.

2.0.4 Strangeness and Charmness enhancement

Another success of the SHM model is the prediction of a phenomenon called strangeness enhancement, which consists of an increase in the production of particles containing strange quarks. In particle production, one would generally expect that the heavier flavours should be suppressed compared to the up and down quarks, both for their greater mass and the need to preserve quantum numbers. In fact it is known that the strong interaction exactly preserves the strangeness quantum number and so the heavier flavours are produced in pairs. Consequently, the production of strange quarks is expected to be suppressed in small collision systems where there is less phase space available for particle production. This because the creation of a second hadron with a compensating strangeness has to be created inside the same small volume at the same time resulting in a large energetic threshold that the system has to overcome (canonical suppression). Instead the fact that the gran canonical formalism, that assumes only the average conservation of the quantum number, is useful for the description of this kind of process tell us that the system behave as if the strange and antistrange hadrons were created independently and statistically distributed over the entire nuclear fireball. This mean that are not important the initial conditions in witch the pairs $s\bar{s}$ are created for determine the final distribution. This point is not completely understood but is probably related to the fact that a significant amount of strangeness diffusion occur before hadronization.

In heavy-ion collisions, the enhancement of strange hadron production is possible due to the high gluon density of the QGP. This is thanks to the dominance of gluonic production channels, such as the processes $gg \rightarrow s\bar{s}$, $u\bar{u} \rightarrow s\bar{s}$ and $d\bar{d} \rightarrow s\bar{s}$. In addition, the partial restoration of the chiral symmetry in proximity to the temperature of deconfined transition reduces the constituent mass thus decreasing the energetic threshold for its production. This effect reduces also the time scale for strangeness saturation that occur for temperatures above 160 MeV, very close to the chemical freeze-out one where the relative particle abundances are fixed. As a consequence, when the quark-gluon plasma breaks up into hadrons, the increased abundance of strange quarks leads to a higher yield of particles containing this flavour in the final state.

Instead the charm quark mass is much larger than the other described in this section and hence thermal production of charm quarks or hadrons is strongly suppressed. However, with increasing center-of-mass energy the

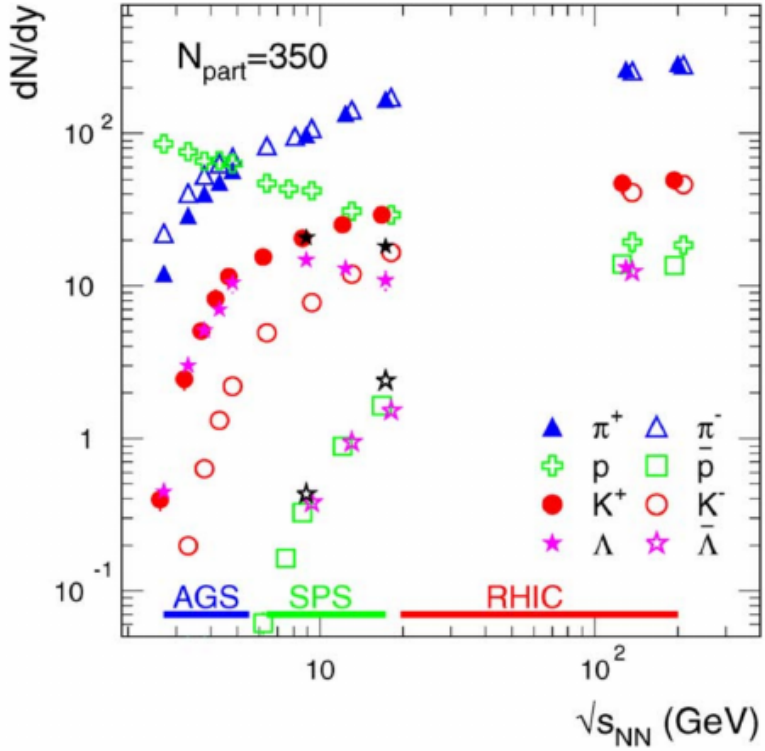


Figure 2.5: The energy dependence of experimental hadron yields at mid-rapidity for various species produced in central nucleus-nucleus collisions. The energy regimes for various accelerators are marked. Note that, for SPS energies, there are two independent measurements available for the Λ hyperon yields [28].

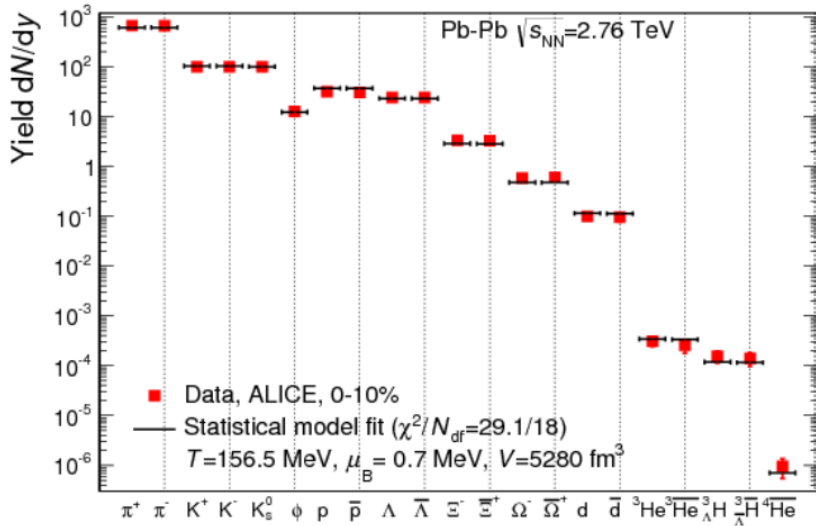


Figure 2.6: hadron multiplicities in central (0-10%) Pb-Pb collisions at the LHC, for different particles [27].

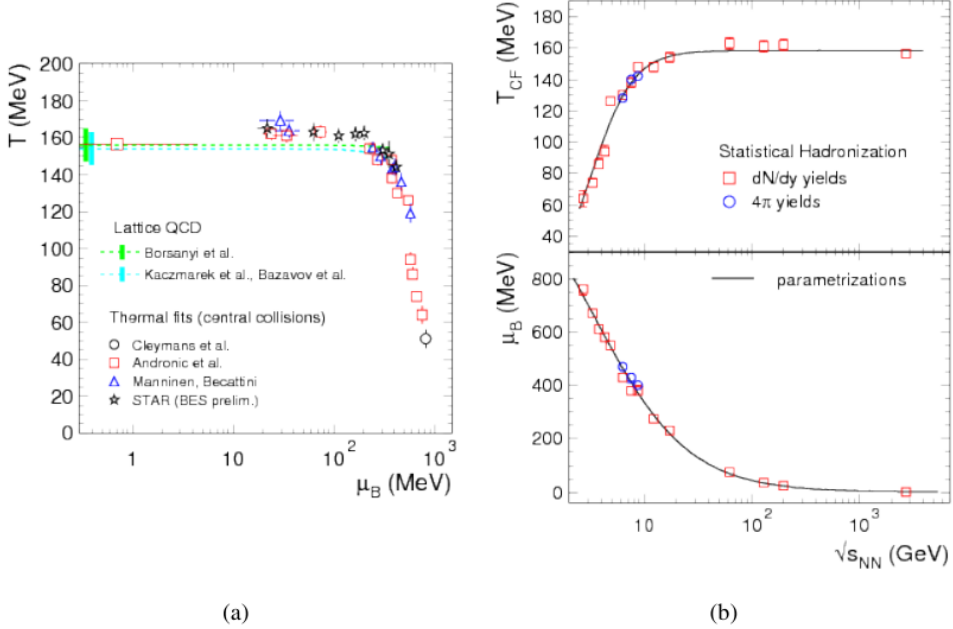


Figure 2.7: The panel (a) show (a) comparison between the Phase diagram of QCD with data points as obtained at different energies and the thermal model fits from SIS up to LHC data. The panel (b) show the evolution of the temperature of chemical freeze-out and the μ_B as a function of the $\sqrt{s_{NN}}$.[27]

total charm production cross section, which results from initial hard collisions, increases strongly. In this case similar considerations made for the strange quark holds also for the heavier charm flavor [29].

Chapter 3

$Y_c\mathbf{N}$ bound state

3.0.1 One Boson exchange model

Before the publication of Hideki Yukawa's groundbreaking papers in 1935 [30], physicists struggled to explain the results of James Chadwick's atomic model, which proposed that protons and neutrons were packed inside a small nucleus with a radius of the order of $10^{-14} - 10^{-15}$ meters. At such small scales, the electromagnetic forces would be extremely intense, causing the protons to repel each other. In 1932, Werner Heisenberg proposed a "Platzwechsel" (migration) interaction between protons and neutrons within the nucleus, suggesting that neutrons were composite particles made of protons and electrons. According to this model, neutrons would emit electrons, creating an attractive force with protons, and then transform back into protons [31]. However, this model violated the conservation of linear and angular momentum. To resolve this issue, Enrico Fermi proposed in 1934 that the emission and absorption of two light particles: the neutrino and electron. A few months later, Soviet physicists Igor Tamm and Dmitri Ivanenko demonstrated that the force associated with the emission of neutrinos and electrons was not strong enough to bind protons and neutrons together in the nucleus.

Yukawa decided so to combine both the idea of short-range force interaction and the idea of an exchange particle in order to explain the neutron-proton binding. by introducing the Yukawa's potential it is possible to start from the Klein-Gordon equation that governs dynamics of free massive scalar, without spin, field

$$\nabla^2 \phi(\vec{r}, t) - \frac{1}{c^2} \frac{\partial^2 \phi(\vec{r}, t)}{\partial^2 t} = \frac{m^2 c^2}{\hbar^2} \phi(\vec{r}, t) \quad (3.1)$$

where ϕ is the wave function, \vec{r} the position, t the time, and m the mass of the particle. In spherical coordinate becomes for the radial component:

$$\frac{1}{r^2} \frac{\partial}{\partial r} (r^2 \frac{\partial}{\partial r} \phi(\vec{r}, t)) - \frac{1}{c^2} \frac{\partial^2 \phi(\vec{r}, t)}{\partial^2 t} = \frac{m^2 c^2}{\hbar^2} \phi(\vec{r}, t) \quad (3.2)$$

A possible solution is:

$$\phi(\vec{r}, t) = -g^2 \hbar c \frac{e^{\frac{i}{\hbar}(\vec{r} \cdot \vec{P} - Et)}}{r} \quad (3.3)$$

Where \vec{P} is the linear momentum and E the energy. For virtual particles holds that $0 \sim p^2 c^2 + m^2 c^4$ so $p \sim \pm imc$ and with the Einstein-De Broglie equation one gets that $\lambda = \frac{\pm i\hbar}{mc}$, named Compton wave length, and the solution can be rewritten rejecting the divergent solution as

$$\phi(\vec{r}, t) = -g^2 \hbar c \frac{e^{-\frac{r}{\lambda}}}{r} = -g^2 \hbar c \frac{e^{-\frac{rmc}{\hbar}}}{r} \quad (3.4)$$

The Eq. 3.4 describes how the mediators of the interaction evolve with time, showing that the massive one produces a short-range interaction due to the exponential decrease. A graphical representation of the phenomena is visible in Fig. 3.1.

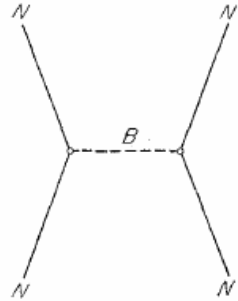


Figure 3.1: The one-boson-exchange diagram of the nucleon-nucleon scattering.

Yukawa used his equation also to predict the mass of the mediating particle in nucleus as about 280 times the mass of the electron ~ 140 MeV. Physicists called this particle the "meson," as its mass was in the middle of the leptons and baryons ones. Yukawa's meson was found in 1947, and came to be known as the pion [4]. This model of interaction based on the exchange of particle is generally called "one-boson-exchange model" (OBE model) or the "one-particle-exchange model". This model has opened up a new possibility for a realistic understanding of nuclear forces; indeed, based on the Yukawa potential, the Sakata model [32] was created with the aim of giving a systematic understanding not only of the nucleon-nucleon interaction but also of other various strong reactions. While the OBE model is extremely useful for understanding the basics of nuclear interactions, it has several important limitations that prevent it from being a complete theory of nuclear forces [33]. Furthermore, the theory has been extended since Sakata's proposal, and some ideas from the model have been incorporated into QCD. However, his introduction was important for understanding the next section.

3.0.2 Λ_c N interaction

This section is a resume of the [34] and [35]. As already seen, the construction of a model to describe non-perturbative QCD phenomena with analytical first-principles calculations is very limited. In addition, the lack of experimental information on $Y_c N$, a bound state of a particle containing a quark charm, in particular for our issue Λ_c , and a nucleon (N), makes its description much more difficult. The situation can therefore be improved by using well-constrained models based as much as possible on symmetry principles and analogies with other similar processes. For this scope an approach was proposed in the early 1990s in an attempt to obtain a simultaneous description of the light baryon spectrum and the nucleon-nucleon interaction [36]. In this model, baryons are described as clusters of three interacting massive (constituent) quarks and is for these reason called Constituent Quark Model (CQM). In this way the microscopic interactions between quarks and gluons are neglected.

According to Goldstone's theorem, when a continuous symmetry is spontaneously broken, new massless scalar particles appear in the spectrum of possible excitations. These particles are called Goldstone bosons and can be thought as the excitations of the field in the broken symmetry directions in group space. This spinless boson can acquire a mass if the symmetry is not exact, like happen for the approximate chiral symmetry, but they typically remain relatively light if compared to other hadrons like protons and neutrons [37]. When the Goldstone bosons are created in the system they can be exchanged by other particle creating a potential. For the chiral symmetry the Goldstone bosons are pions (π) and their chiral partner (σ) and the complessive potential take the form:

$$V_\chi = V_\sigma(\vec{r}_{ij}) + V_\pi(\vec{r}_{ij}) \quad (3.5)$$

where

$$V_\sigma(\vec{r}_{ij}) = \frac{-g_{ch}^2}{4\pi} \frac{\Lambda^2}{\Lambda^2 - m_\sigma^2} m_\sigma \left[Y(m_\sigma r_{ij} - \frac{\Lambda}{m_\sigma}) Y(\Lambda r_{ij}) \right] \quad (3.6)$$

$$\begin{aligned} V_\pi(\vec{r}_{ij}) &= \frac{g_{ch}^2}{4\pi} \frac{m_\pi^2}{12m_i m_j} \frac{\Lambda^2}{\Lambda^2 - m_\pi^2} m_\pi \left[Y(m_\pi r_{ij} - \frac{\Lambda^3}{m_\pi^3}) Y(\Lambda r_{ij}) \right] \vec{\sigma}_i \cdot \vec{\sigma}_j \\ &+ \left[H(m_\pi r_{ij}) - \frac{\Lambda^3}{m_\pi^3} H(\Lambda r_{ij}) \right] S_{ij}^2(\vec{\tau}_i \cdot \vec{\tau}_j) \end{aligned} \quad (3.7)$$

$\frac{g_{ch}^2}{4\pi}$ is the chiral coupling constant, m_i are the masses of the constituent quarks, $\Lambda \sim \Lambda_{CSB} = 4\pi f_\pi \sim 1\text{GeV}$ a momentum scale where f_π is the pion electroweak decay constant, $Y(x) = \frac{e^{-x}}{x}$ is the standard Yukawa function, $H(x) = (1 + \frac{3}{x} + \frac{3}{x^2})Y(x)$, $S_{ij} = 3(\vec{\sigma}_i \cdot \hat{r}_{ij})(\vec{\sigma}_j \cdot \hat{r}_{ij})\vec{\sigma}_i \cdot \vec{\sigma}_j$ is the quark tensor operator with σ the Pauli matrices. For an explicit expression of the parameters and their expectation values see [35]. The meson exchange potential

contains four kinds of terms: spin-independent, spin-spin, spin-orbit, and tensor. The spin-independent term is the one that has the greatest influence on the depth and shape of the potential well at not too small distances and for this reason it will be studied in more detail in the following section. The spin operator also includes the Pauli repulsion, producing an increasing repulsive effect as the distance between the hadrons decreases; this becomes essential for the fermion description. It's possible to see that this term will become significant in determining which configuration between nucleons is most plausible to be observed. The spin-orbit and tensor contributions can instead be thought as effects analogous to magnetism, due to the presence of relative motion in the colour charges (colour-magnetism effect). The latter will then contribute in the case where the total angular momentum of the bound state is not zero. Perturbative QCD effects are taken into account through the one-gluon-exchange (OGE) potential that take the form:

$$V_{OGE}(\vec{r}_{ij}) = \frac{\alpha_s}{4} \vec{\lambda}_i^c \cdot \vec{\lambda}_j^c \left[\frac{1}{r_{ij}} - \frac{1}{4} \left(\frac{1}{2m_i^2} + \frac{1}{2m_j^2} + \frac{2\vec{\sigma}_i \cdot \vec{\sigma}_j}{3m_i m_j} \right) \frac{e^{-r_{ij}/r_0}}{r_0^2 r_{ij}} \frac{3S_{ij}}{4m_i m_j r_{ij}^3} \right] \quad (3.8)$$

where $\vec{\lambda}^c$ are the SU(3) color matrices, $r_0 = \hat{r}_0/\nu$ is a flavor-dependent regularization scaling with the reduced mass ν of the interacting pair, and α_s is the scale-dependent strong coupling constant given by:

$$\alpha_s(\nu) = \frac{\alpha_0}{\ln[(\nu^2 + \mu_0^2)/\gamma_0^2]} \quad (3.9)$$

$\alpha_0=2.118$, $\mu_0 = 36.976$ MeV and $\gamma_0=0.113$ fm $^{-1}$. the Eq. 3.9 gives rise to $\alpha_s \sim 0.54$ for light quark and $\alpha_s \sim 0.43$ for uc pairs. The table 3.1 resumes all the parameters.

$m_{u,d}$ (MeV)	313	$g_{ch}^2/4\pi$	0.54
m_c (MeV)	1752	m_σ (fm $^{-1}$)	3.42
\hat{r}_0 (MeV fm)	28.170	m_π (fm $^{-1}$)	0.70
μ_c (fm $^{-1}$)	0.70	Λ (fm $^{-1}$)	4.2
b (fm)	0.518	a_c (MeV)	230

Table 3.1: The table summarizes the typical values of the parameters present in the previous equation.

Finally, any model imitating QCD should incorporate confinement. Although it is a very important term from the spectroscopic point of view, it is negligible for the hadron-hadron interaction. Lattice QCD calculations suggest a screening effect on the potential when increasing the interquark distance which is modeled here by.

$$V_{CON}(\vec{r}_{ij}) = -\alpha_c (1 - e^{-\mu_c r_{ij}}) \vec{\lambda}_i^c \cdot \vec{\lambda}_j^c \quad (3.10)$$

The Fig. 3.1 shows the different diagrams contributing to the charmed baryon-nucleon interaction. The first type of interaction, visible in (a) and (b), is mediated by the exchange of a boson between light quark or between a light ad heavy flavor. The second one instead takes into account also the exchange of the identical light quark (c) and (d). The last possibility (d) correspond to short range interaction based on one-gluon exchange contributions not present in the interaction in ordinary nucleus because of the only presence of light flavours. In the limit where the two baryons Λ_c N overlap, the Pauli principle impose antisymmetry requirements. Such effects, if any, will be prominent for relative S waves ($L = 0$). The S wave normalization kernel of the two-baryon wave function can be written in the overlapping region ($R \rightarrow 0$)

$$N \rightarrow 4\pi \left(1 - \frac{R^2}{8} \left(\frac{5}{b^2} + \frac{1}{b_c^2} \right) \right) [1 - 3C(S, I) + \dots] \quad (3.11)$$

Where $C(S, I)$ is a spin-isospin coefficient and b, b_c are the parameters for the wave function of the light and charmed quarks, respectively, assumed to be different for the sake of generality. The closer the value of $C(S, I)$ to $1/3$ the greater is the suppression at short distances of the wave function, generating Pauli repulsion, effect visible in the phase shift. So there might exist Pauli suppressed channels.

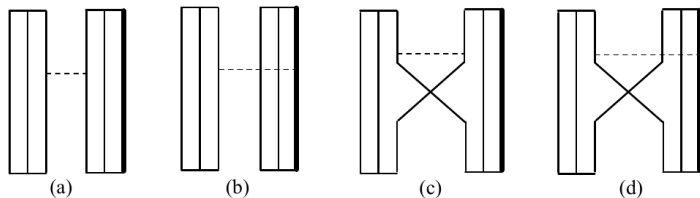


Figure 3.2: The vertical solid lines represent a light quark, u or d. The vertical thick solid lines represent the charm quark. The dotted horizontal lines stand for the exchanged boson. The different type of interaction are: (a) Interaction between two light quarks. (b) Interaction between the heavy and a light quark. (c) Interaction between two light quarks together with the exchange of identical light quarks. (d) Interaction between the heavy and a light quark together with the exchange of identical light quarks.

A numerical simulation of the potential is described in [38], performed with lattice QCD with lattice spacing $a = 0.0907(13)$ fm and physical lattice size $La = 2.902(42)$ fm. The Fig. 3.3 shows the $\Lambda_c N$ central potential in the 1S_0 channel with different masses considered for the pion. For ensemble 1 $m_\pi \sim 700$ MeV, $m_\pi \sim 570$ MeV for ensemble 2 and 410 MeV for ensemble 3. They found a repulsive interaction at short distances ($r < 0.5$ fm) and an attractive one for intermediate distances ($0.5 < r < 1.5$ fm). The same calculation has also been performed with a $\Lambda_c N$ system with $J^P = 1^+$ obtaining the result visible in the Fig. 3.4. The two results are qualitatively and quantitatively

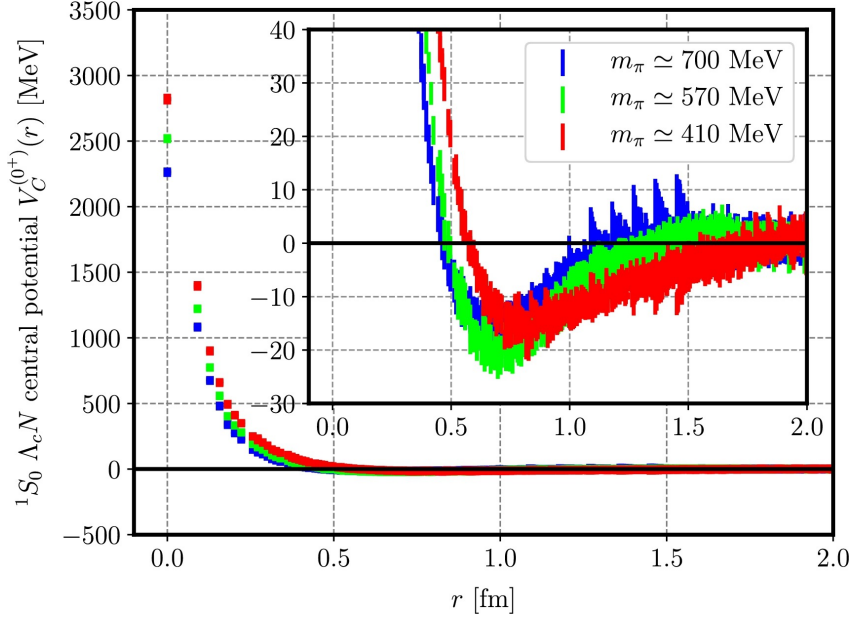


Figure 3.3: The figure show $\Lambda_c N$ central potential in the 1S_0 channel for each ensemble. The potential is calculated for $m_\pi \approx 700$ MeV case (Blue), for $m_\pi \approx 570$ MeV case (Green) and for $m_\pi \approx 410$ MeV case (Red).

similar except at short distance ($r < 0.5$ fm). As can be seen for both $\Lambda_c N$ S waves the intensity of the attraction becomes stronger as the pion mass decreases, moving towards the predictions of the CQM. However the 3S_1 potential is more attractive than 1S_0 . This is due to the short-range dynamics consequence of gluon and quark exchange. In fact, if no meson exchanges were considered, the S wave phase shifts of the $\Lambda_c N$ system are very similar to the corresponding NN scattering. Instead considering the exchange both partial waves are subjected by hard-core phase shifts due to the short-range gluon and quark-exchange dynamics. However, the hard-core radius in the spin-singlet state is larger than in the spin-triplet one leading to a more attractive interaction in the spin-triplet partial wave due to a lower short-range repulsion. In fact, the hard cores caused by the color magnetic part of the OGE potential have been calculated obtaining 0.35 fm for the spin-triplet state and 0.44 fm for the spin-singlet one.

In conclusion is possible to note that the potential of $\Lambda_c N$ system is less attractive with respect to other hyper-nucleus like ΛN , this fact could be explained from the following consideration.

- The long-range contribution is expected to be caused by the K meson exchange for ΛN interaction. In the system, however, the K meson (strange quark) exchange is replaced by the D meson (charm quark) exchange. This contribution is highly suppressed due to the significantly larger mass of the D meson compared to the K meson.

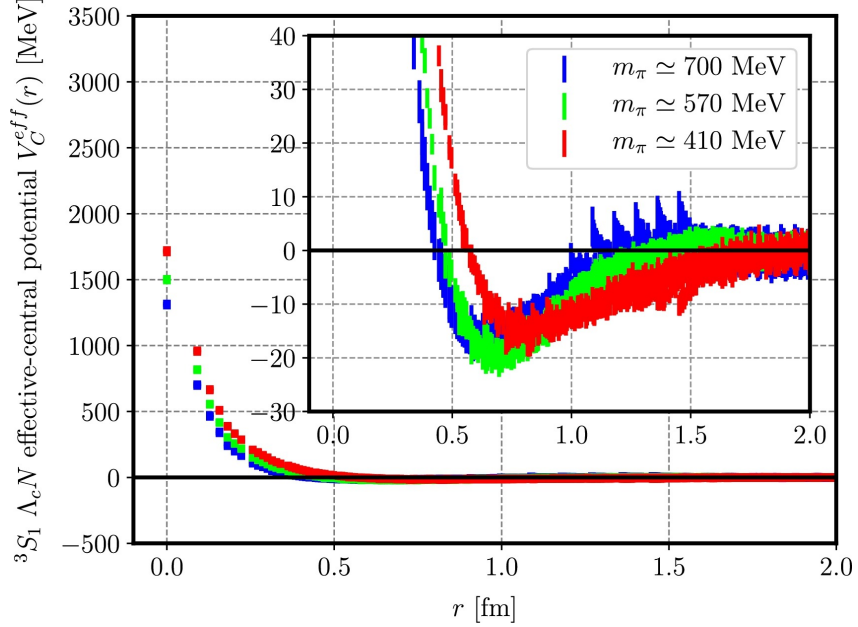


Figure 3.4: The figure show $\Lambda_c N$ central potential in the 3S_1 channel for each ensemble. The potential is calculated for $m_\pi \approx 700$ MeV case (Blue), for $m_\pi \approx 570$ MeV case (Green) and for $m_\pi \approx 410$ MeV case (Red).

- The one-pion exchange in the $\Lambda N - \Sigma N$ transition is considered to give a contribution to the effective ΛN interaction. Instead this contribution is expected to be suppressed due to the large mass difference between $\Lambda_c N$ and $\Sigma_c N$.

3.0.3 Possible Λ_c super-nuclei

One of the most interesting applications of the charmed baryon-nucleon interaction is the study of the possible existence of super-nuclei. A description of the potential had been taken from [38]. Since the Λ_c interaction is dominated by the spin-independent central force, as we discussed in the previous section, the spectrum of super-nuclei, if they exist, would probably be approximated by the following single-folding potential defined by:

$$V_f(\vec{r}) = \int d^3r' \rho_A(\vec{r}') V_{\Lambda_c N}(\vec{r} - \vec{r}') \quad (3.12)$$

Where $\rho_A(\vec{r})$ denotes the nuclear density distribution corresponding to the atomic number A and $V_{\Lambda_c N}$ stands for the two body spin-independent central potential of the Λ_c system. The study described assumed,

$$\rho_A(\vec{r}) = \rho_0 \left[1 + e^{\frac{r-c}{a}} \right] \quad (3.13)$$

Where the parameters employed ρ_0 , c, a are the same used for describing spherical nuclei such as ${}^{12}C$, ${}^{28}Si$, ${}^{40}Ca$, ${}^{58}Ni$ and ${}^{208}Pb$. With the following

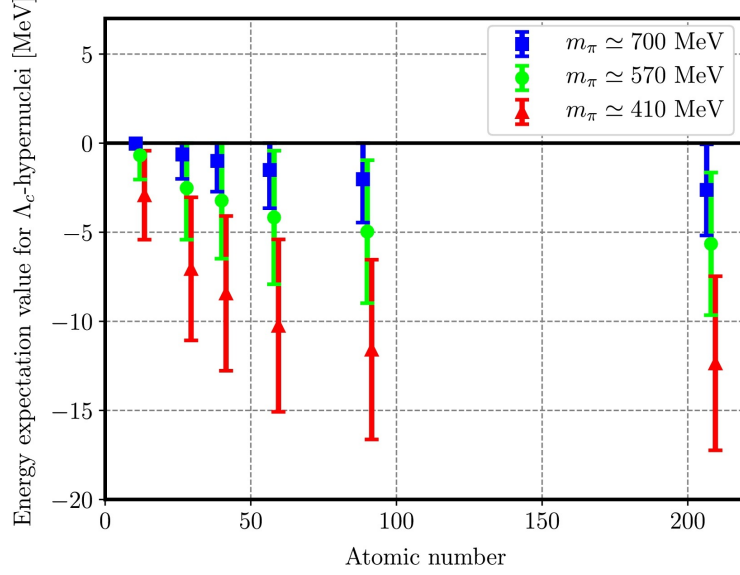


Figure 3.5: The figure show the binding energy in symmetric nuclei with the parameter assumed for each atomic number for each ensemble. The binding energies are calculated from the folding potentials for Λ_c super-nuclei by using the Gaussian expansion method. The folding potentials are constructed from the spin-independent central potential of the $\Lambda_c N$ system

potential they calculate the binding energy for Λ_c super-nuclei by the Gaussian expansion method for the S-wave potential. The result is shown in Fig. 3.5. As expected the binding energy increases with increasing atomic number. Furthermore varying the mass of the quark up and down in the simulation is observed that when their masses decrease toward physical values, and so the potential approach the physical one, the binding energy increases. These results suggest super-nuclei may exist, if their binding energy is larger than the Coulomb repulsion energy. To calculate the expectation value for the Coulomb potential energy they used a potential defined by:

$$V_C(\vec{r}) = \int d^3 r' \rho_{ch}(\vec{r}') V_{Coulomb}(\vec{r} - \vec{r}') \quad (3.14)$$

Where $V_{Coulomb}$ is an ordinary Coulomb potential and ρ_{ch} is the charge density distribution obtained from elastic electron scattering for the previous nucleus. It is interesting to compare the energy expectation values, also taking Coulomb repulsion into account; the result is shown in Fig. 3.6. It's possible to see that for heavy nuclei the repulsion is too weak but for $A = 12-58$ the expectation values for the Coulomb force are not much stronger than the binding energy of Λ_c super-nuclei.

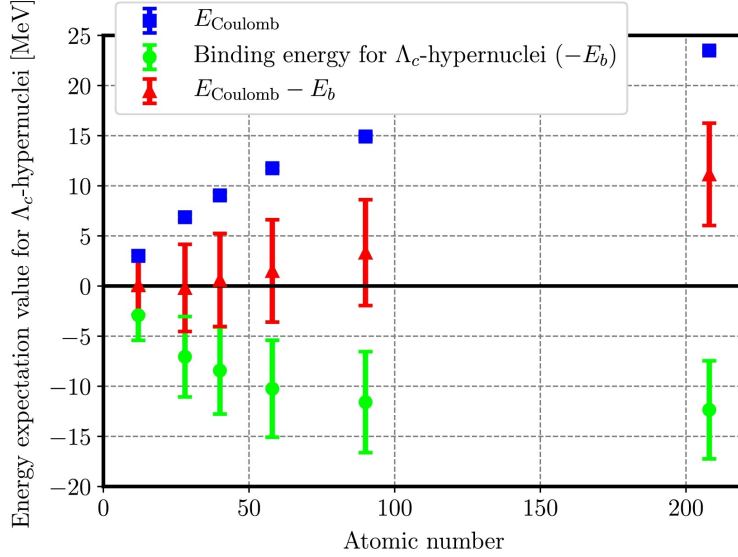


Figure 3.6: The figure show the expectation value of folding potential for Coulomb force in Λ_c super-nuclei (Blue). The expectation values are calculated from the binding solution of the Λ_c super-nuclei for Ensemble 3 ($m_\pi \approx 410$ MeV). For comparison, the binding energy of Λ_c super-nuclei (Green) and sum of them (Red) are also plotted.

3.0.4 C-deuteron ($c-d$) simulation

Using the SHM model, we investigated how the production of super-nuclei depends on various parameters. In particular, we focused on the c-deuteron, denoted $c-d$ for convenience, which is a bound state of a Λ_c and a neutron. This choice is motivated by the fact that the c-deuteron is the most accessible super-nucleus to search for in heavy-ion collisions due to its mass. In fact, it is the lightest bound state of a Λ_c and a nucleon without Coulomb repulsion which makes the existence of this super-nucleus less likely.

The first step was the $c-d$ characterization. The most probable configuration for its existence was chosen, i.e. the 3S_1 state, so that the associated spin is $1 \hbar$. The mass was obtained by adding the mass of the $\Lambda_c = (2286.46 \pm 0.14)$ MeV/ c^2 and the neutron mass $m_n = 939.56542052(54)$ MeV/ c^2 [39] removing then the binding energy. The latter value is still unknown, for this reason the binding energy of the deuteron was used, $E_{be\,d} = (2.224575 \pm 0.000009)$ MeV [40], giving $m_{c-d} \approx 3.223$ GeV/ c^2 . One would expect a lower effective $c-d$ binding energy, but as can be seen in Fig 3.5, the order of magnitude is correctly identified. Furthermore, since the binding energy is of the order of MeV while the estimated mass is of the order of GeV/ c^2 the effect of this approximation is negligible for the purpose of the present analysis.

We then started the simulation using the Thermal FIST [41], with a grand-canonical formalism based on Maxwell-Boltzmann statistics, thus neglecting quantum mechanical effects, for all particles except mesons, for which Bose-

Einstein statistics were used due to their abundance. The focus was on central collisions, so a spherically symmetric shock wave momentum spectrum was assumed. For each combination of parameters, $2 \cdot 10^7$ events were generated, setting the typical chemical potential observed in LHC collision. The baryonic potential was set at $\mu_B = 0.71$ MeV and the electric charge potential was fixed at $\mu_Q = -0.18$ MeV as described in [9] for Pb-Pb collisions at $\sqrt{s_{NN}} = 5.02$ TeV in ALICE¹. Instead, as described in [25], at the same energy in the center of mass the charm fugacity was $\gamma_c = 29.6 \pm 5.2$, however, this parameter was particularly important in determining the expected abundance of $c - d$, so it was changed in a second step. On the other hand, the chemical potential of strangeness has no influence on the following considerations since no particle with a strange quark had been analyzed and was therefore set to zero.

At the end of the generation, a histogram of the multiplicity dN/dy as a function of y was obtained. The integral was then evaluated using discrete values in order to determine the total particle yield at mid-rapidity ($|y| < 0.5$). For the rapidity variable y , a half-bin width was taken as the uncertainty, corresponding to 0.006 in all the simulations. In contrast, the uncertainty on dN/dy was provided directly by the simulation program. Finally, for the hadron masses and their associated uncertainties, the values reported in [39] were used.

The number of nuclei generated versus rapidity was then plotted in a semi-logarithmical scale for a chemical freeze-out temperature of 156 MeV and a radius of 8 fm in the range $|y| < 0.5$, obtaining the result shown in Fig. 3.7. It can be observed that the number of particles produced in a collision decreases exponentially with increasing mass. Moreover, the phenomenon of charm enhancement becomes evident in the higher abundance of particles containing a charm quark compared to what would be expected for particles of the same mass, as illustrated by the fit lines. The function used for the fit was of the form $dN/dy = ae^{bx}$, where a and b are free parameters. For nuclei without quark charm, the values obtained are $a = (1.057 \pm 0.014) 10^5$ while $b = (6.2107 \pm 0.0071) \text{ GeV}^{-1}$ with a $\tilde{\chi}^2 = 0.16$. The value of $\tilde{\chi}^2$ turns out to be particularly low, most likely due to the large number of events considered, which reduces the statistical uncertainty. On the other hand, for particles containing a charm quark it was not possible to proceed in the same way, since the production of Λ_c baryons is more strongly affected by the presence of resonances, as discussed in [29]. For this reason, the previously determined coefficient b was fixed in the fit, and only the parameter a was extracted, yielding $a = (3.534 \pm 0.021) 10^5$, in particular for the $c - d$, $(dN/dy)_{c-d} = (7.072 \pm 0.042) \cdot 10^{-4}$. These results reinforce the earlier observation of strangeness enhancement, as particles containing heavier flavors appear more abundant than expected. For a more complete picture see Fig. 3.8 in which the color code separates particles with 1, 2, 3 charm quarks. The line at the far left corresponds to particles without a quark charm and coin-

¹The measured values were $\mu_B = 0.71 \pm 0.45$ MeV while $\mu_Q = -0.18 \pm 0.90$ MeV

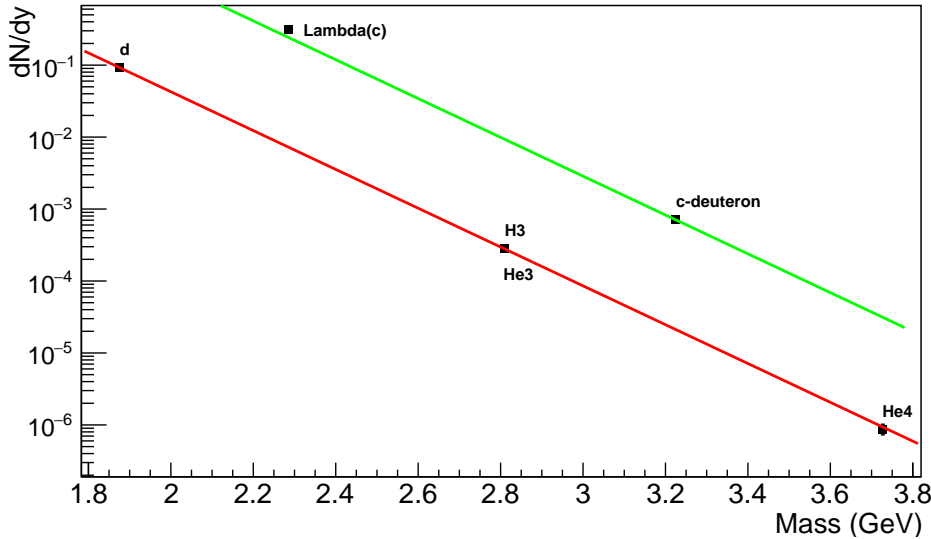


Figure 3.7: The figure shows the value of dN/dy of different hadrons in mid-rapidity with the temperature of freeze-out fixed at 156 Mev and the freeze-out radius at 8 fm with a logarithmic scale on the y axis. The two line show the different fit performed for the nucleus and the hadrons with a quark charm.

cides with that determined for (u,d,s) hadrons. In this graph is more evident how the deviation clearly visible for a single quark charm is due to feeding from hadronically unstable resonances. The data presented in the graph suggest that, based solely on midrapidity $c-d$ production, the expected abundance could be sufficient for detection with the ALICE detectors. However, as discussed later and in Section 4.4, other factors may interfere with its detection, making its identification more challenging.

We then started to change the value of the temperature of chemical freeze-out and his radius. We have considered temperatures in the range of 150 MeV to 160 MeV with unit steps of increment in order to see how the number of particles produced would change locally by setting the freeze-out radius at 8 fm. A similar procedure was followed varying the volume by considering freeze-out radii from 4 to 12 fm with unit increments and a fixed freeze-out temperature set at 156 MeV. Fig. 3.9 shows the combined effects of volume and temperature variations. It can be seen that the number of expected $c-d$ increases more rapidly with increasing volume than is observed for temperature. However, it's necessary to pointed out that the percentage changes in radius, and therefore in volume, made during the simulation are much larger than those for temperature.

Analyzing in more detail the results on the variation of the radius, the expected increase in the $c-d$ abundance was predictable from the Eq. 2.25, in fact assuming a spherical symmetry the trend $dN/dy \propto r^3$ = was expected; therefore, the fit was performed with a relation $dN/dy = ar^3 + b$, with a

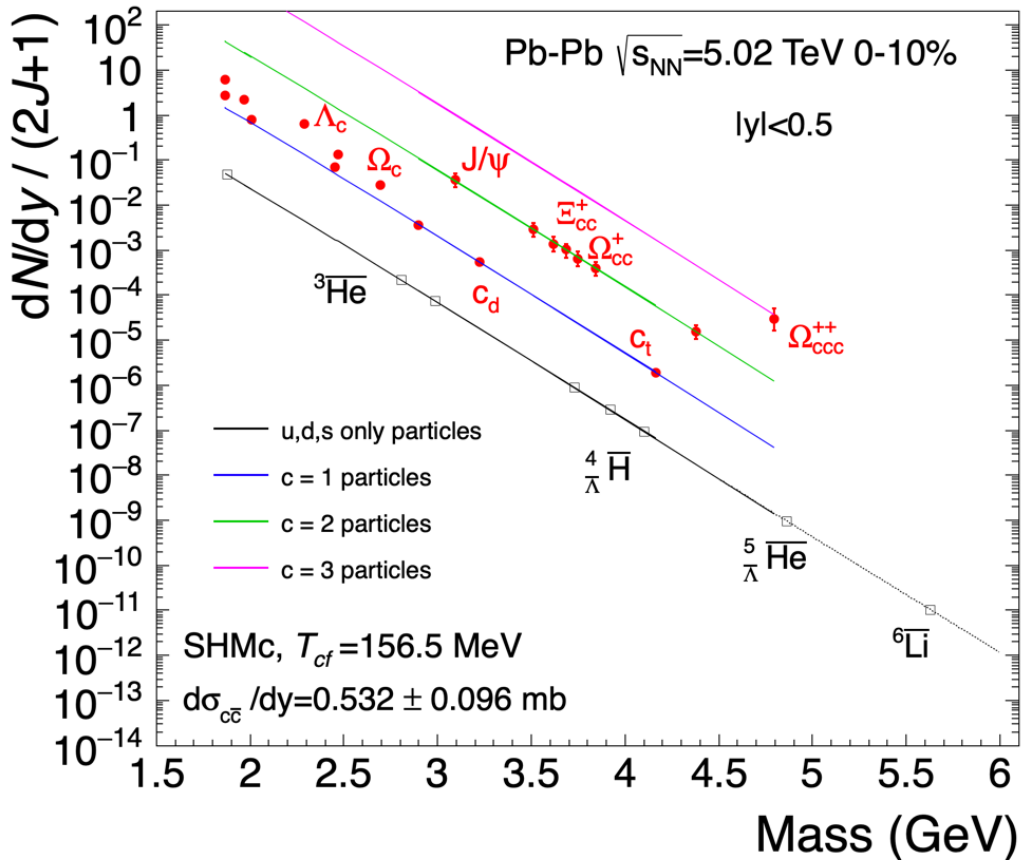


Figure 3.8: The figure shows the value of dN/dy of different hadrons in mid-rapidity with the temperature of freeze-out fixed at 156 Mev and the freeze-out radius at 8 fm. The color code separates particles with 1, 2, 3 charm quarks while the line at the far left corresponds to particles without a quark charm.

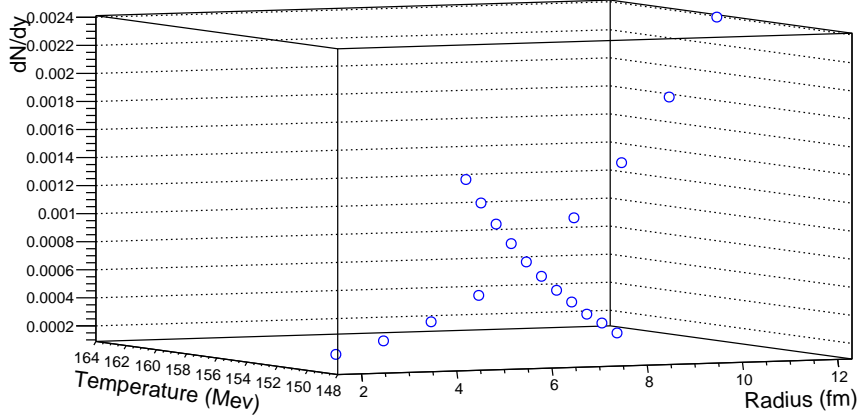


Figure 3.9: The figure show the value of dN/dy of $c - d$ in the range $|y| < 0.5$ obtained from the simulation with a freeze-out temperature fixed at 156 Mev for variation in the radius and a radius of 8 fm for changing in the temperature.

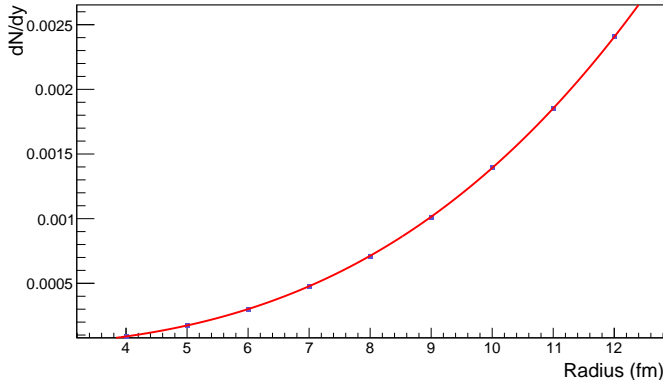


Figure 3.10: The figure show the value of dN/dy of $c - d$ in the range $|y| < 0.5$ obtained from the simulation with a freeze-out temperature fixed at 156 MeV.

and b fit parameters. The Fig 3.10 show the results of the fit confirming the prediction. The fit results are $a = (1.3921 \pm 0.0032) 10^{-6} \text{ fm}^{-3}$, $b = (2.43 \pm 0.13) 10^{-8}$ with $\tilde{\chi}^2 = 0.42$. The former number suggest that the functional dependence has been correctly identified.

With regard to the evaluation of temperature increase, the expected trend was not easy to predict, but Eq. 2.13 seems to suggest an exponential trend. The result of the fit is shown in Fig 3.11. The functional relation that best described the data produced was of the form $dN/dy = ae^{bT} + c$, with a, b and c parameters to be determined; the reason for this trend is unclear and could only be a local behaviour of a more complex functional relation. The values obtained from the fit are $a = (1.19 \pm 0.17) 10^{-12}$, $b = (0.13009 \pm 0.00087) \text{ MeV}^{-1}$ and $c = (-6.38 \pm 0.50) 10^{-6}$ with a $\tilde{\chi}^2 = 1.0$. The lat-

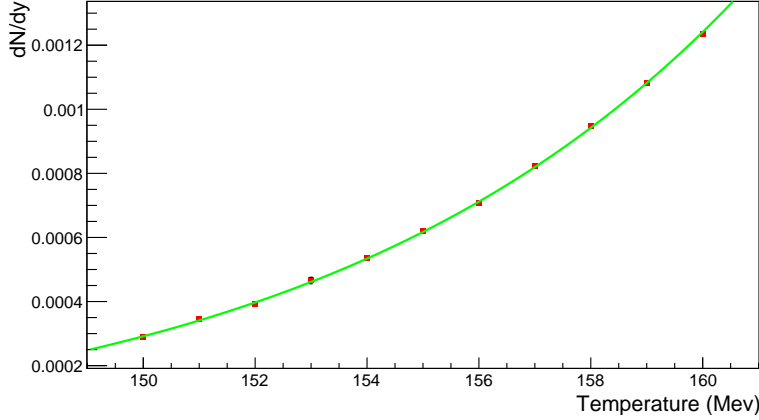


Figure 3.11: The figure show the value of dN/dy of $c - d$ in the range $|y| < 0.5$ obtained from the simulation with a freeze-out radius fixed at 8 fm.

ter value suggests that although it was not possible to proceed analytically from Eq. 2.25, the agreement with the empirical relationship is nevertheless consistent. This result also supports the earlier observation that increases in temperature produce, at least locally, exponential increases so although Fig. 3.9 may suggest that changes in radius are more effective this is related to the larger variations in percentage that were used in the analysis described so far.

An attempt was then made to investigate how variations in the charm fugacity affect the final result. Once again, it is possible to make an analytical prediction, starting from Eq. 2.25.

$$\begin{aligned}
 \langle N \rangle &= \frac{\Delta V g_i}{2\pi^2 \hbar^3} \int_0^\infty dp \frac{p^2}{e^{-\beta(\mu_i - E)} + \theta_i} \\
 &\approx \frac{\Delta V g_i}{2\pi^2 \hbar^3} \int_0^\infty dp p^2 e^{\beta(\mu_i - E)} \\
 &= \frac{\Delta V g_i}{2\pi^2 \hbar^3} e^{\beta \mu_i} \int_0^\infty dp p^2 e^{-\beta E} \\
 &\propto \gamma_c
 \end{aligned} \tag{3.15}$$

In the first step, it was assumed to be in the classical limit, where the Maxwell-Boltzmann distribution can be applied, given the large mass of the super-nucleus under study, and then the contribution of the chemical potentials was removed from the integral, since they were fixed during the simulation. A linear increase was therefore expected, so to verify the prediction of the model, $2 \cdot 10^7$ events were generated with unit increments of the charm fugacity from 24.6 to 36.6, to cover the range of values most likely to occur during an experiment at the LHC. For greater generality, the relationship used for the fit was of the form $dN/dy = ax + b$ and the results obtained were $a = (2.366 \pm 0.032) \cdot 10^{-5}$, $b = (2.53 \pm 0.94) \cdot 10^{-5}$ and a $\tilde{\chi}^2 = 1.4$. Again, the agreement suggests that the functional relationship has been correctly

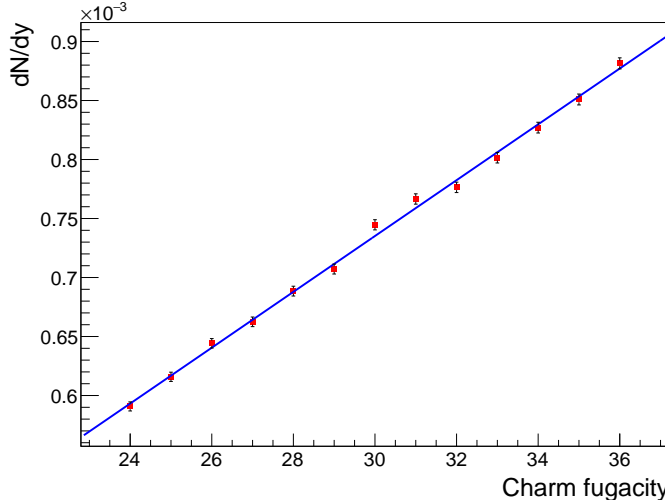


Figure 3.12: The figure show the value of dN/dy of $c - d$ in the range $|y| < 0.5$ obtained from the simulation with a freeze-out temperature fixed at 156 Mev and a radius set at 8 fm.

identified. The fit results are visible in Fig 3.12, in this case a slightly worse agreement is observed but this is probably related to the lower scale in the y axis. Furthermore, if the number of charm quarks in a bound state increase, one would expect from Eq. 3.15 $a \propto (\gamma_c)^\alpha$ trend with α number of charm quarks present.

We finally analyzed the detection of $c - d$. Based on the data obtained from the previous simulations, a histogram was produced to correlate the momenta of $c - d$ with its occurrence. Then, using a Monte Carlo simulation with PYTHIA 8 [42], $c - d$ were generated with a distribution of the linear momentum based on our previous results. The decays leading to the formation of a deuteron were then examined in order to estimate the increase in the number of deuterons originating from super-nucleus decay. The decay channels included in the simulation, together with their branching ratios, are summarized in Tab. 3.2. It is important to note that after the decay of Λ_c , the resulting decay proton will bind to the remaining neutron only with a probability, estimated by a coalescence model, of 3-10%. Specifically, only protons with a relative momentum in the rest frame of the nucleus below a threshold of 200 MeV/c are bound [43]. The total branching ratio for the $c - d$ decay in the deuteron is then given by the product of the branching ratio of the different channels analyzed multiplied by the aforementioned probability, assumed to be 7%, of the proton to bind to the neutron. Since the formation of the deuteron by the channel in which the Λ_c arrived in a Λ and then in a proton is suppressed by the double decay, that reduce the possibility of create bound state, this process are not be taken into account in this evaluation.

Thus, by generating random numbers with a hit-or-miss approach, we

Channel	Branching ratio
d K^0	(2.3 ± 0.6)% x 7%
d $K^- \pi^+$	(5.0 ± 1.3)% x 7%
d $\bar{K}^*(892)$	(1.6 ± 0.5)% x 7%
d $K^0 \pi^0$	(3.3 ± 1.0)% x 7%
d $K^0 \eta$	(1.2 ± 0.4)% x 7%
d $K^0 \pi^+ \pi^-$	(2.6 ± 0.7)% x 7%
d $K^- \pi^+ \pi^0$	(3.4 ± 1.0)% x 7%
total	(1.36 ± 0.39)%

Table 3.2: The table shows all the decay channels used for the analysis. The first column shows the possible decays product, and the second one the branching ratios with their relative error; x 7% means that the branching ratio should be reduced by the probability of forming a bound. In this case, d stands for deuteron.

estimated the probability of detecting a deuteron originating from the $c - d$ decay. Regarding the efficiency of detection the value related to the estimate track finding efficiency of ALICE 3 reported in Fig. 4.7 has been used, for more details see Section 4.4. Out of a total of 10^9 simulated $c - d$ decays, the number of deuterons produced by the decays was $(1.55449 \pm 0.00039) \cdot 10^7$, while the fraction actually detected was $N_{detect} = (5.4823 \pm 0.0023) \cdot 10^6$. Therefore, the probability of detecting a deuteron produced by $c - d$ decay is estimable as $p_D = \frac{N_{detect}}{10^9} = (5.4823 \pm 0.0023) \cdot 10^{-3}$. We can see that the previous values are consistent with what was expected, since the fraction of deuterons produced should be of $\sim 1.4\%$ of the total events number, and the average detection efficiency should be of about 40%. In conclusion, the number of detected deuterons coming from $c - d$ decay has been estimated under the following assumptions:

- the number of collision performed by LHC are $N_{LHC} = 10^{10}$;
- only the central collisions have been considered, assumed to be $p_{central} = 5\%$ of the total;
- the freeze-out temperature is 156 MeV with a freeze-out radius of 8 fm and a charm fugacity of 29.6 under spherical symmetry;
- abundances are derived only from the decay channels listed in Tab. 3.2;
- the probability of a bound state formation after the decay is 7%;
- only $c - d$ with $|y| < 0.5$ were considered.

Under these conditions, the expected number of detected deuterons is:

$$N_D = (1938 \pm 12) \text{ deuterons.}$$

This value has been estimated by:

$$N_D = N_{LHC} \cdot p_D \cdot (dN/dy)_{c-d} \cdot \Delta y \cdot p_{central} \quad (3.16)$$

Since only $|y| < 0.5$ is considered, we take $\Delta y = 1$. To calculate the uncertainty on N_D , the quantities p_D and $(\frac{dN}{dy})_{c-d}$ are assumed to be independent, so:

$$\sigma_{N_D}^2 = \left(\frac{\partial N_D}{\partial p_D} \right)^2 \sigma_{p_D}^2 + \left(\frac{\partial N_D}{\partial (\frac{dN}{dy})_{c-d}} \right)^2 \sigma_{(\frac{dN}{dy})_{c-d}}^2 \quad (3.17)$$

$$\sigma_{N_D} = N_D \cdot \sqrt{\left(\frac{\sigma_{p_D}}{p_D} \right)^2 + \left(\frac{\sigma_{(\frac{dN}{dy})_{c-d}}}{(\frac{dN}{dy})_{c-d}} \right)^2} \quad (3.18)$$

This value seems to indicate the real possibility of finding $c - d$, although, since it is such a high value, the fact that it has not yet been observed may suggest that this bound state does not actually form. However, the assumptions are very restrictive and this value can be considered as a lower limit of the expected contribution.

Chapter 4

ALICE

The A Large Ion Collider Experiment (ALICE) is a detector designed for heavy-ion physics at the Large Hadron Collider (LHC). It is primarily used to study lead-lead (^{208}Pb) collisions and so the most severe design constraint is to be able to withstand the high charge multiplicity expected for central events. During a collision conditions similar to those just after the Big Bang are recreated, condition that may also be present in neutron stars and other astrophysical objects. The ALICE collaboration uses the 10 000-tonne ALICE detector 26 m long, 16 m high, and 16 m wide. The detector sits in a vast cavern 56 m underground close to the village of St Genis-Pouilly in France, receiving beams from the LHC [44]. The aim of ALICE is to recreate and study quark-gluon plasma, which is crucial for understanding the mechanisms that confine quarks and gluons, chiral symmetry restoration and the nature of the strong nuclear force. ALICE is currently the only experiment at the LHC specifically designed to study nuclear matter produced in relativistic heavy-ion collisions and the QGP. For this reason, it must be able to measure as many observables as possible by studying all the different phenomena that can be attributed to the formation of a QGP state. It can estimate parameters such as the charged multiplicity of the interactions, the impact parameter, the shape and orientation of the fireball, the collision volume and the number of nucleons interacting in the collision. Almost all known Particle IDentification (PID) techniques are used in ALICE, such as: specific energy loss (dE/dx), time-of-flight, Cherenkov radiation, electromagnetic calorimetry, muon detectors and topological reconstruction of decays. Despite all these identification techniques, it's very difficult to select signals of decays of heavy flavours, as will be explained in the last section, so the acquisition of a huge amount of data with a high efficiency of the data acquisition system (up to a frequency of 1.3 GB/s) is required.

A sketch of the ALICE coordinate system is shown in Fig. 4.1. In this figure, the (x, y, z) axes are shown together with the cylindrical coordinates used to describe the trajectory of particles in ALICE, (r, θ, φ) .

The ALICE sub-detectors are categorized into two main groups: one at

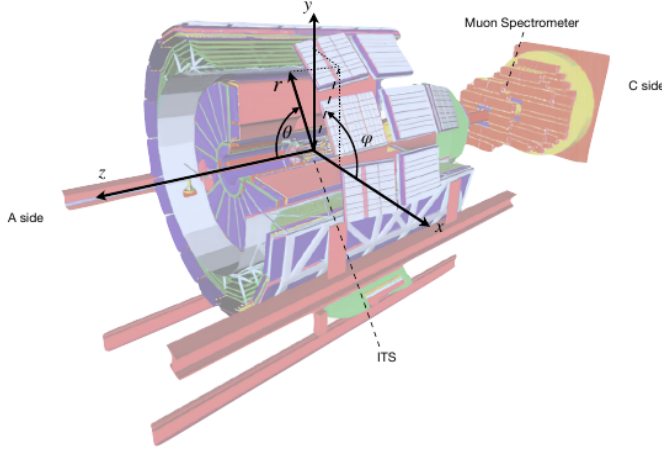


Figure 4.1: The figure show the cylindrical coordinate set used to describe the position of the objects with respect the cartesian one [7].

mid-rapidity $|\eta| < 1$, the central barrel, and one at forward rapidity $-4 < \eta < -2.5$, that include also the muon spectrometer for muon identification. The apparatus scheme can be resumed in the following manner.

- The central barrel detectors can measure all over the azimuthal angle and are embedded in the L3 solenoid magnet, providing a maximum magnetic field strength of 0.5 T. It includes in order from the interaction point and going outward [14] [15]:
 1. The **Inner Tracking System (ITS)** is a silicon tracking system composed of six cylindrical layers. Its main goal is to identify the position of the primary vertex with a resolution better than $100 \mu\text{m}$ and provide tracking of charged particles.
 2. The **Time Projection Chamber (TPC)** is used for tracking of charged an particle identification.
 3. The **Transition Radiation Detector (TRD)** is composed of stacks of gas chamber and radiators to identify and track electrons.
 4. The **Time of Flight (TOF)** measure the time of flight providing important information for particle identification. It can also provide a trigger specific for cosmic ray and Ultra Peripheral Collision (UPC) events.

These subsystems are mostly dedicated to vertex reconstruction, tracking, particle identification and momentum measurement. Are also present some specialized detectors with limited acceptance.

1. **High-Momentum Particle Identification Detector (HMPID)** is used to identify charged particles with $p_{\perp} > 1 \text{ GeV}/c$.

2. **PHOton Spectrometer (PHOS)** is an electromagnetic calorimeter used for photons identification and as high-energy photon trigger.
 3. **ElectroMagnetic Calorimeter (EMCal)** is a Pb-scintillator calorimeter for identify photons and pion with $\eta < 0.7$ and it is also used as jet trigger.
 4. **Di-jet Calorimeter (DCal)** is an electromagnetic calorimeter specifically designed to extend the acceptance of the EMCal and enable back-to-back correlation measurements.
- The forward detectors include:
 1. **Muon spectrometer** for reconstruct heavy quark hadrons thought their weak decays in the channels $\mu^-\bar{\nu}_\mu$ or $\mu^+\nu_\mu$ or for electrodynamical decay in $\mu^+\mu^-$ pairs.
 2. **Forward Multiplicity Detector (FMD)** composed by several layers of silicon strip detectors at a distance of $70 \div 150$ cm from the interaction point.
 3. **Photon Multiplicity Detector (PMD)** made of preshower detectors and proportional counters.
 4. **Zero Degree Calorimeters (ZDC)** a proton and neutron calorimeter.
 5. **V0 Detectors** made of two scintillator arrays for triggering and luminosity and centrality measurements.
 6. **T0 detectors** is a Cherenkov counter for event time measurement.

In the following section we will discuss some of the most important one. A schematic view of the ALICE detector is reported in Fig. 4.2.

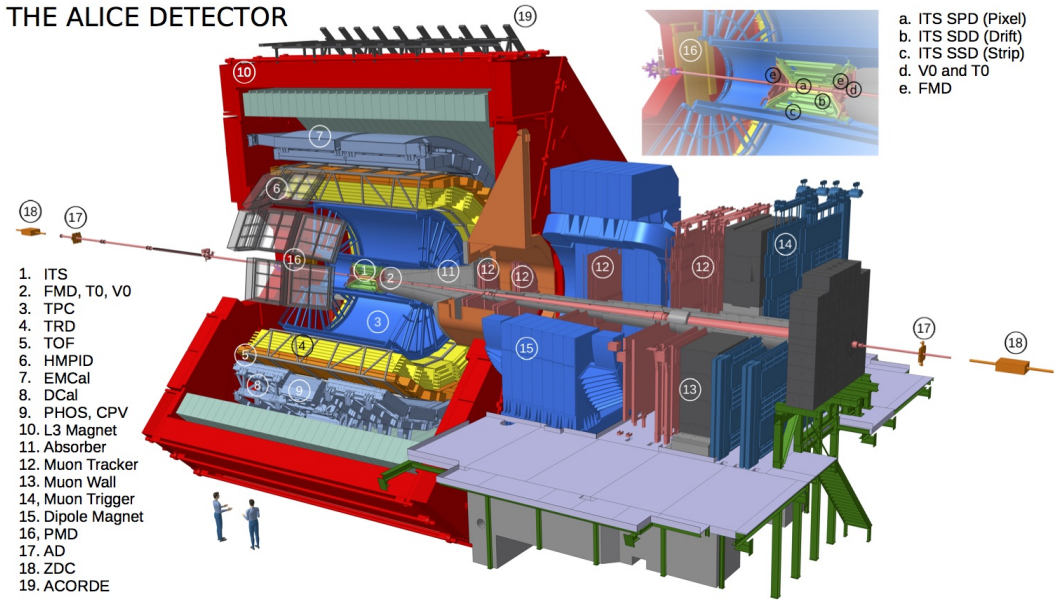


Figure 4.2: The figure show the Layout of the ALICE detector in Run2 with their position and dimension [45].

4.1 Central barrel

4.1.1 Inner Tracking System (ITS)

The Inner Tracking System (ITS) is a crucial part of the ALICE tracking system, positioned as the innermost sub-detector of the central barrel, closest to the beam pipe and the interaction point. It consists of six concentric cylindrical layers of silicon detectors, comprising two layers each of Silicon Pixel Detector (SPD), Silicon Drift Detector (SDD), and Silicon Strip Detector (SSD) as visible in Fig 4.3. The ITS covers the pseudorapidity region $|\eta| < 0.9$ for interactions occurring within 10 cm from the nominal interaction point. The SPD is located at radial distances of 3.9 cm and 7.6 cm from the beam axis. These layers cover extended pseudorapidity ranges of $|\eta| < 2.0$ and $|\eta| < 1.4$, respectively. They consist of hybrid silicon pixel detectors, in total $9.8 \cdot 10^6$, which generate binary signals when traversed by charged particles, facilitating their counting. The primary functions of the SPD are to determine the position of the primary vertex with a high resolution, better than $100 \mu\text{m}$, to help isolate events coming from pileup, and to contribute to the triggering system due to their fast response. The SPD also contributes to achieving an impact-parameter resolution better than $50 \mu\text{m}$ for tracks with transverse momentum $p_\perp > 1.3 \text{ GeV}/c$. The two intermediate layers are the SDD, situated at radii of 15.0 cm and 23.9 cm, covering $|\eta| < 0.9$. The SDD has very good multi-track capability and provides two out of the four measurements of specific dE/dx employed for PID by the ITS. It provides two-dimensional spatial information ($r \phi$ and z) with a spatial resolution of $35 \mu\text{m}$.

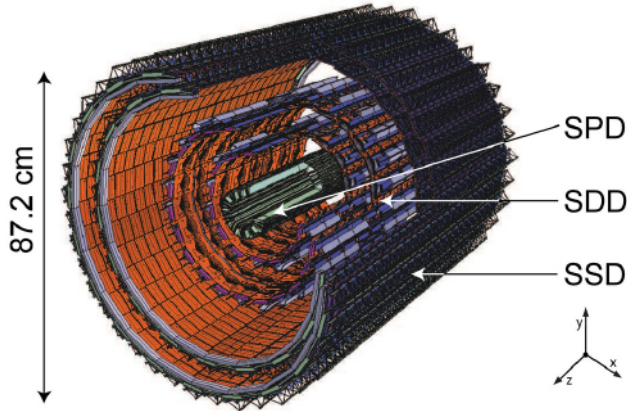


Figure 4.3: Schematic diagram of the Inner Tracking System (ITS) of the ALICE experiment [46].

($r \phi$) and $25 \mu\text{m}$ (z). The SDD determines particle positions using drift time estimation and charge centroid measurement; for this reason it is structured with a central cathode for more precise particle tracking. The two outermost layers employ double-sided Silicon Strip Detectors, located at radial distances of 38.0 cm and 43.0 cm , covering $|\eta| < 1.0$. The SSD is essential for the prolongation of tracks from the main tracking detector of ALICE, the Time Projection Chamber, to the ITS. It provides a spatial resolution of $20 \mu\text{m}$ ($r \phi$) and $830 \mu\text{m}$ (z) and $27 \mu\text{m}$ ($r \phi$) and $830 \mu\text{m}$ (z), with a readout time of $1 \mu\text{s}$. Besides connecting tracks, the SSD also provides dE/dx information. The ITS can also perform "standalone" tracking for charged particles in the low p_\perp region by using exclusively the information from its six layers [14] [11] [47] [15].

4.1.2 Time Projection Chamber (TPC)

The Time Projection Chamber is the main tracking detector of the central barrel. It is specifically designed for measure tracks in the transverse momentum range $0.1 - 100 \text{ GeV}/c$ and pseudorapidity range $|\eta| < 0.9$. It is positioned at radial distances ranging from 85 to 247 cm from the beam axis, extending along the beam direction with a total length of 510 cm . It is divided along the beam axis into two equally large drift regions by a central cathode, each having a length of 2.5 m . On the opposite sides of the central electrodes there is the readout plate, which is equipped with multi-wire proportional chambers (MWPC). Each of the 18 readout chambers covers an azimuth of 20° ; a graphical resume is visible in Fig. 4.4. The volume of the TPC ($\sim 90 \text{ m}^3$) can be filled with different gases depending on the running conditions. The perfect candidate is a gas with a small radiation length and low multiple scattering rates, so is usually filled with a mixture containing various

combinations of argon, neon, carbon dioxide and sometimes nitrogen. When charged particles pass through the gas, they ionize it, creating an electron-ion pairs. These ionization electrons then drift towards sensing electrodes under a uniform electric field, typically achieved by applying a high voltage of around 100 kV between the central electrode and the readout plates. The ionization electrons drift with a speed of approximately 2.7 cm/s, corresponding to a maximum drift time of around 92 ms. This drift process allows spatial localization of the ionization event along the particle trajectory. In addition, the presence of a uniform magnetic field along the z-direction causes charged particles to bend into curved trajectories, a graphical resume is visible in Fig. 4.5. The position resolution for the inner/outer radii ranges from 800 to 1100 μm in the transverse plane ($r \phi$) and from 1100 to 1250 μm along the beam axis (z). The total charge collected at the end plates for each track is proportional to the particle energy loss in the gas. This allows a sampling of the dE/dx and therefore perform PID below 1 GeV/c. The resolution on the dE/dx is 5% for isolated tracks (low multiplicity collisions), while when the number of particles increases such as Pb–Pb collisions (high multiplicity collisions), the resolution is 7%. This is due to the increased probability to have hits close in space. In addition, the contribution of positive ions to the signal shape increases with the particle occupancy and the formation of large amount of charged particles can induce local modifications to the electric field modifying the drift speed and complicating the reconstruction of the track. The specific energy loss can be described by the Bethe-Bloch formula, which depends on the particle species, its momentum, and the properties of the traversed medium. It can be estimate in the following manner proposed by [48]:

$$f(\beta) = \frac{P_1}{\beta^{P_4}} \left(P_2 - \beta^{P_4} - \ln(P_3) \frac{1}{(\beta\gamma)^{P_5}} \right) \quad (4.1)$$

Where β is the particle velocity in c unit, γ the Lorentz factor, P_{1-5} free parameter that must be estimate from data [14] [11] [47] [15].

4.1.3 Transition Radiation Detector (TRD)

The Transition Radiation Detector (TRD) is positioned between the TPC and TOF detector and it covers a pseudorapidity range of $|\eta| < 0.84$. It is principally used for electron identification in the high momentum region ($p > 1 \text{ GeV}/c$), where discriminating between electrons and pions using traditional dE/dx techniques becomes challenging. When charged particles attempt to cross the detector, they pass through two media with different dielectric constants thus emitting transition radiation with an intensity proportional to their Lorentz factor. Since different particles have different masses and velocities, they emit different amounts of transition radiation making the identification possible [14] [11].

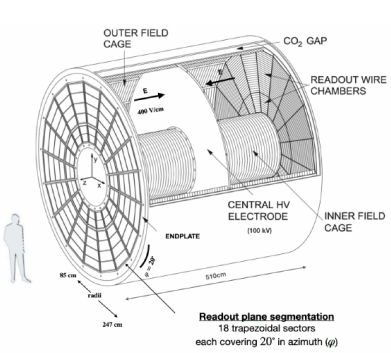


Figure 4.4: The figure show a schematic representation of the time projection chamber [49]

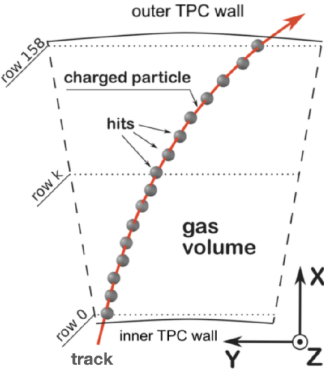


Figure 4.5: The figure show a diagram of the TPC tracking method [50]

4.1.4 Time Of Flight (TOF)

The Time Of Flight (TOF) detector is a large array of Multi-gap Resistive-Plate Chambers (MRPC), located between 3.7 m and 3.99 m radial distance, from the interaction point. It is designed to identify charged particles produced in pseudorapidity of $|\eta| < 0.9$ and with an intermediate momentum range ($0.5 < p_{\perp} < 4$ GeV/c). In addition TOF has been used to provide a trigger specific for cosmic ray and UPC events. The TOF detector has a modular structure divided along the azimuthal direction into 18 supermodules as visible in Fig. 4.6. If a particle ionizes the gas in the detector, an avalanche process will be triggered to generate signal on the readout electrodes. Particle identification is performed by combining the reconstructed momentum (p) and track length (l) with the measurement of the time of flight (t) in TOF. The mass (m) corresponding to the one of the detected particle can be obtained as.

$$p = m\gamma\beta c \longleftrightarrow m = \frac{p\sqrt{1 - \beta^2}}{c\beta} = \frac{p\sqrt{\frac{1}{\beta^2} - 1}}{c} \quad (4.2)$$

The β parameter can be measured in the following manner

$$\beta = \frac{v}{c} = \frac{l}{c t} \quad (4.3)$$

So

$$m = \frac{p\sqrt{\left(\frac{l}{c t}\right)^2 - 1}}{c} \quad (4.4)$$

It can be shown that, at large momenta, the resolution on the track momentum (σ_p) becomes negligible and the total uncertainty is driven by the uncertainties on the timing (σ_t) and track length (σ_l). For this reason, an MRPC-based TOF was designed, as such detectors have been shown to be able to achieve

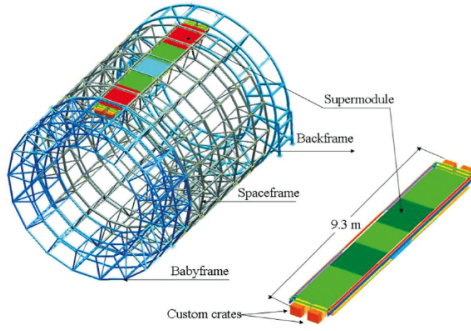


Figure 4.6: The figures show the structures of the time of flight detector [51].

a time resolution better than 50 ps with an efficiency close to 100% [14] [11] [47]. .

4.1.5 Photon Spectrometer (PHOS)

The Photon Spectrometer (PHOS) is an electromagnetic calorimeter known for its high spatial and energy resolution thanks to a scintillating material called Lead Tungstate ($PbWO_4$). It covers a pseudo-rapidity range of $|\eta| < 0.12$ with a dynamic energy range from 0.1 GeV to 100 GeV. Its main goal is to measure QGP temperature, space-time dimensions and study deconfinement through jet quenching [14] and [11].

4.1.6 High-Momentum Particle Identification Detector (HMPID)

The High Momentum Particle Identification Detector (HMPID) is dedicated to the identification of charged hadrons with $p_{\perp} > 1$ GeV/c, thus extending the PID capabilities of the ITS, TPC and TOF at high momentum. It covers a pseudorapidity range of $-0.6 < \eta < 0.6$ and consists mainly of two parts: the radiator and the photon detector composed by seven Ring Imaging Cherenkov (RICH) counters [14] and [11].

4.1.7 Electromagnetic Calorimeter (EMCal)

The EMCal consists of towers of $6 \times 6 \times 20$ cm 3 each, made up of 76 alternating layers of lead and scintillator (not uniform, unlike PHOS). It was designed to measure electrons from the decay of heavy flavour hadrons, but not only. It also identifies high-energy particles and enhances energy resolution across various momenta, enabling precise measurements of jet quenching, high-energy jets, and high-momentum electrons and photons [14] and [15].

4.2 Forward Detectors

VZERO detector (V0)

The V0 detector consists of two circular arrays of scintillator counters (named V0A and V0C) one per side with asymmetric distance from the interaction point. The V0A covers the pseudorapidity region $2.8 < \eta < 5.1$ while V0C $-3.7 < \eta < -1.7$. They are important both in pp collision and AA collision for the following reasons:

- **Triggering:** The V0 detector provides a minimum bias trigger signal. This is important because it helps to detect a broad range of inelastic collision events without introducing significant selection bias.
- **Rejection background events:** The VZERO detector helps in the rejection of background events generated by interaction of beams with residual gas within the beam pipe and with mechanical structures. This is possible thanks to the time gap between signals from V0A and V0C.
- **Centrality determination:** The signal given by the V0 detector is proportional to the number of particles traversing it, thus providing information about the multiplicity and centrality of the collision. These data are precious for understanding the collision geometry and interpreting experimental results accurately [14] and [11].

4.2.1 T0 Detectors

The T0 detector consists of two arrays, T0A and T0C, of Cherenkov counters placed along the beam pipe on each side of the interaction point, respectively at -72.7 cm and 375 cm. The pseudorapidity coverage are $4.61 < \eta < 4.92$ (T0A) and $-3.28 < \eta < -2.97$ (T0C). Its primary function is to provide a fast timing signal for the TOF detector, serving as a collision time reference. It can be also used for an independent determination of the vertex position along the beam axis (with a precision of ± 1.5 cm) [14] and [11].

4.2.2 Zero Degree Calorimeter (ZDC)

The Zero Degree Calorimeter (ZDC) consists of four calorimeters, two for protons (brass-quartz proton ZP) and two for neutrons (tungsten-quartz neutron ZN), located at ~ 112.5 cm away from the interaction point, symmetrically in both directions. The ZDC measures the energy of the spectator nucleons and assists in the estimation of centrality and luminosity in heavy-ion collisions by determining the collision geometry, overlap regions of the colliding nuclei and the number of participating nucleons [14] and [11].

4.2.3 Muon Spectrometer

The muon spectrometer is located 14 m in the negative beam direction and covers a pseudorapidity range of $2.5 < \eta < 4$. It helps to study the complete spectrum of heavy quarkonia via their decay in the $\mu^+\mu^-$ channel. It is composed of different parts. The particles cross first an absorber, mainly composed of carbon and concrete, designed to absorb the hadrons emerging from the interaction point. This material choice is for limit the multiple scattering and the energy loss of the muons. The muons then traverse five tracking stations and are deflected by the magnetic field allowing for the determination of their momentum. The dipole magnet provides a magnetic field nominally of $B = 0.7$ T but can be changed by the requirements on the mass resolution. The next part is the muon filter, an iron wall designed to reduce the background in the trigger chambers by absorbing secondary hadrons and low momentum muons. Finally, the muons reach the trigger system, which consists of two stations equipped with resistive plate chambers characterized by a time resolution of about 1 ns [14], [52] and [7].

4.3 ALICE upgrades

The ALICE Collaboration has proposed a significant detector upgrades and a completely new apparatus, named ALICE 3, for the LHC Runs 3, 4 and 5, respectively. These upgrades will enable new measurements in the heavy-flavour sector, focusing on low p_\perp , especially for measuring multi-charm baryon production, multi-differential measurements of dielectron emission, as well as femtoscopic studies of the interaction potentials between heavy mesons [47]. The upgrade program includes the installation of an improved Inner Tracking System and a new Muon Forward Tracker for faster and more precise particle tracking and vertexing, enabled in part by a smaller diameter beampipe. New timing detectors called Fast Interaction Triggers (FIT) have replaced the forward detectors. Additionally, the MWPC has been replaced by quadruple-Gas Electron Multiplier (GEM) chambers as readout chambers of the TPC. These replacements were motivated by the requirement to preserve the particle identification capabilities of the TPC at significantly higher interaction rates. In fact with these upgrades the readout rate achieves a significant increase rising from approximately 1 kHz to 50 kHz.

ALICE 3 is a compact, next-generation multipurpose detector that will replace the current ALICE detector after the LHC Long Shutdown 4 (2034-2035). The aim is to build a nearly massless barrel detector consisting of truly cylindrical layers based on curved wafer-scale ultra-thin silicon sensors with Monolithic Active Pixel Sensor (MAPS) technology, featuring an unprecedented low material budget of 0.05% X_0 per layer, with the innermost layers positioned inside the beam pipe thanks to a retractable design. In addition to superior tracking and vertexing capabilities over a wide momentum range

down to a few tens of MeV/c, the detector will provide particle identification via time-of-flight determination with about 20 ps resolution, and with a RICH detector.

For the study of the heavy-flavor sector, the Muon Forward Tracker (MFT) plays a crucial role. In particular it is useful in estimating the degree of thermalization of heavy quarks via the measurement of the elliptic flow of charmonia and single muons from decays of heavy-flavor hadrons. Furthermore, the MFT extends the tracking of charged particles to the forward region, which was not possible in ALICE before its installation. It is made of two half-cones, each cone containing five detection half-disks perpendicular to the beam axis, between $z = -460$ mm and $z = -768$ mm and cover the pseudorapidity region $-3.6 < \eta < -2.5$. MFT provides a pointing resolution of a few tens of μm for muons at forward rapidity, as well as secondary vertexing for muon pairs by matching the tracks reconstructed in the Muon Spectrometer to those reconstructed in the MFT. The MFT uses a silicon pixel chip called the ALice PIxel DEtector (ALPIDE). The various ALPIDE chips are glued on flexible printed circuits to form ladders, which are then assembled onto the half-disks. A total of 936 ALPIDE chips equip the MFT, covering a total surface of around 0.4 m^2 [7].

4.4 Track and vertex reconstruction

To reconstruct particle's trajectory a tracking algorithms is used [47]. This process employs the Kalman filter algorithm, which uses the information contained in a data cluster and transforms them into tracking information to obtain the best possible approximation of the real trajectory. It is implemented in a three-pass tracking scheme known as inward-outward-inward.

The tracking procedure starts with the clustering step performed separately by each detector in witch, starting from the raw data, clusters are created. The clusters are groups of hits produced by a single particle interaction with a detector element and contain its positions, signal amplitudes, signal times and their associated errors. Then the first inward stage starts. As a first step, the track seeds are built from the clusters of the two outermost pad rows of the TPC and the primary vertex point as a constraint. For determine the interaction vertex the information provided by the SPD detector plays a crucial role because is closest to the interaction point, and has excellent transverse plane resolution due to its high granularity. The resolution of the SPD vertex is of $10 \mu\text{m}$ in Pb–Pb collisions and $150 \mu\text{m}$ in pp collisions at $\sqrt{s_{NN}} = 7 \text{ TeV}$. To find the vertex position the algorithm searches the space point that minimises the distance among the tracklets, which are the track segments reconstructed by associating pairs of clusters in the two SPD layers, localizing the point where most of the tracklets converge. When pileup interaction is expected, like in the high multiplicity events, the algo-

rithm is repeated several times, discarding at each iteration those clusters which contributed to already-found vertices. When the primary vertex has been localized the algorithm starts to search the tracklets that fulfill certain proximity cuts trying to reconstruct the path from the interaction vertex and the data of the TPC. Sometimes happen that the same physical track is reconstructed multiple times; to mitigate this issue, a dedicated algorithm is used to identify pairs of tracks that share a fraction of common clusters above a certain threshold, typically ranging from 25% to 50%. The efficiency of the track reconstruction process is influenced by the transverse momentum of the tracks and drops below $p_{\perp} < 0.5 \text{ GeV}/c$, as visible in Fig. 4.7 due to energy loss in the detector material, while for higher p_{\perp} the efficiency is affected by the path followed, as it may pass through areas where clusters are lost due to dead zones between read sectors [14]. In the second step the tracks reconstructed thanks to the TPC are used as seeds for the propagation of the outer tracks. As these seeds are propagated inward, they are continuously updated by incorporating clusters within a defined proximity cut. In this way a tree of track hypothesis is created using the new seed generated by each update. The final candidates are selected based on their $\tilde{\chi}^2$ penalizing the case in which clusters are not found during the extrapolation except for the passage in the dead zones of the detector. In the last stage, the reconstructed tracks are propagated starting from the outer TPC radius toward the interaction point for refine the track parameter. Finally the Kalman filter provides the track parameters including: position, direction, and inverse curvature, with the associated covariance matrix.

The MFT has been designed to allow a clean identification of muon sources, resulting in particular in the possibility of having charm/beauty separation and background reduction in the light-flavor sector. The MFT tracking algorithm can be separated into two steps: the track finding and the track fitting. For the track finding two methods are used. The first one is called Linear Track Finder (LTF) that looks for cluster position aligned along a straight line although the magnetic field curves the trajectory of charged particles, but the deviation can be neglected at least at high p_{\perp} . For help in these work a radial tolerance Rcut is given, a graphical resume is visible in Fig. 4.8. If a track has been recognized in the previous step the corresponding clusters are removed from the list of available ones and are no more considered. The next step consists on a Cellular Automaton (CA) approach particularly suited for low-momentum tracks. It is based on a propagation and joining of consecutive tracklets. So starting from a given segment, considered as the first, the algorithm search the further ones imposing track continuity conditions. The strategy is visible in Fig. 4.9. Only after that the track candidates are found, a track fitting algorithm is applied in order to extract the kinematic parameters. It is able to determine the spatial and momentum coordinates considering material effects [7].

Once the tracks and the interaction vertex have been found a search for

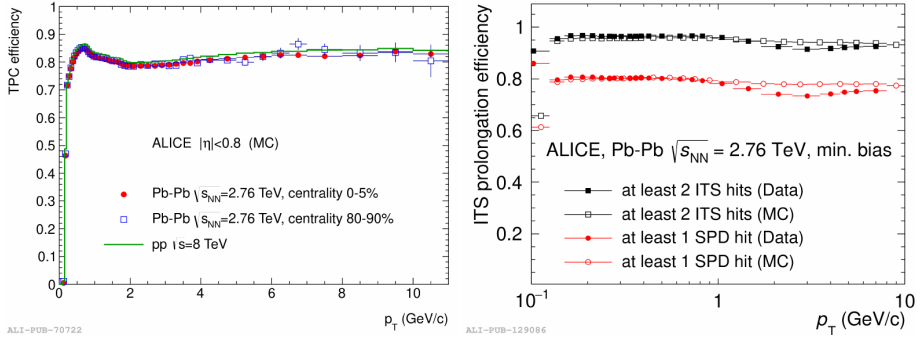


Figure 4.7: Track finding efficiency for primary particles in different types of collision [51]. On the left panel: reconstruction efficiency for TPC tracks in Pb-Pb collision at $\sqrt{s_{NN}} = 2.76$ TeV. Right panel: matching efficiency of tracks from ITS to TPC in real, full markers, and simulated, open markers, Pb–Pb collisions at $\sqrt{s_{NN}} = 2.76$.

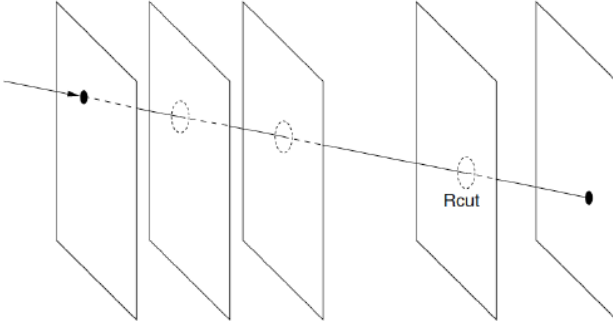


Figure 4.8: The figure show Linear Track Finder schematic using the RCut parameter [53]

photon conversions and secondary vertices from particle decays is performed. In ALICE, secondary vertex reconstruction begins by selecting tracks with Distance of Closest Approach DCA greater than 0.5 mm in pp collisions or 1 mm in Pb–Pb collisions. A schematic view of the reconstruction procedure is reported in Fig. 4.11. For each pair of selected tracks with opposite charges, known as V0 candidates, the following additional selection criteria are also applied:

1. The distance between the two tracks at their PCA is requested to be less than 1.5 cm;
2. The PCA is requested to be closer to the interaction vertex than the innermost hit of either of the two tracks;
3. The cosine of the angle between the total momentum vector of the pair and the line connecting the primary and secondary vertex must be greater than 0.9.

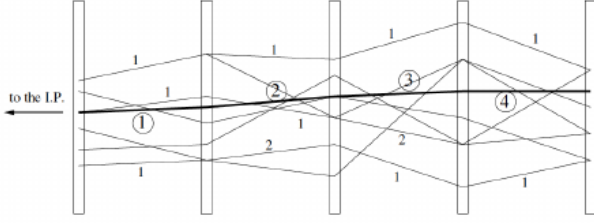


Figure 4.9: The figure show how the Cellular Automaton method works [53].

For V^0 candidates with a momentum below 1.5 GeV/c the cut are relaxed. For the study of heavy-flavor decays close to the interaction point, the secondary vertex is searched starting from point that satisfied other different topological condition [51]. The secondary vertices are then reconstructed with the same algorithm used to compute the primary vertex from tracks. The resolution on the position of secondary vertex can be estimated by Monte Carlo simulations to be of the order of 100 μm with little p_T -dependence for $p_T > 1 \text{ GeV}/c$ [54]. For this reason it is particularly difficult to detect particles with charm flavour, because for example the Λ_c has a mean life of $t = (2.024 \pm 0.031) 10^{-13} \text{ s}$, so it can move away from the interaction point for $ct \approx 60 \mu\text{m}$, less than the instrument resolution. For this reason it is impossible to clearly distinguish the two vertices, making the analysis much more complex. Using the decay of the $c - d$ in the $\Lambda_c \rightarrow pK\pi$ channel the study [43] tried to evaluate the ALICE 3 performance for reconstructing $c - d$ decay using a fast simulation. They show that the distance of closest approach resolution of ALICE 3 allows a very effective suppression of this background, as shown in Fig. 4.10. In contrast to this, the correlated background in which a deuteron from a true $c - d$ decay picks up a wrong pion or kaon is negligible. So assuming the production rates of the statistical-thermal model, central collisions and the previous evaluate spectrum of p_T for the $c - d$ about 50 occurrence per month of Pb–Pb running is achieved. It can be concluded that ALICE 3 is well suited to either discover or rule out the existence of these states.

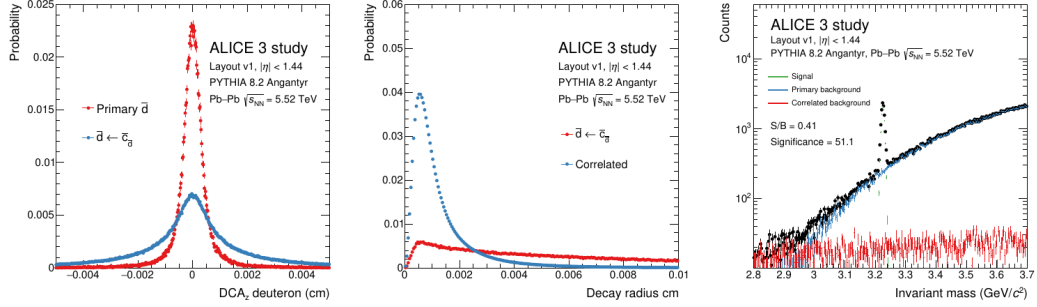


Figure 4.10: On the left, the distribution of the distance of closest approach for primary deuterons and deuterons from c-deuteron decays is shown. In the middle the decay radius for signal and correlated background and on the right the distribution of the invariant mass, correlated background and background from primary deuterons reshown.

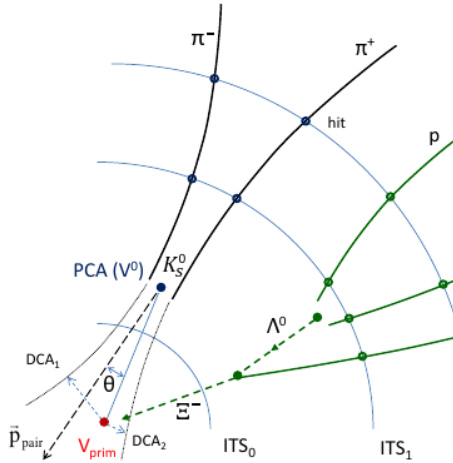


Figure 4.11: The figure shows the secondary vertices reconstruction procedure for different particles. Is possible to observe that long-lived particles detected are used for reconstructing by back-propagating the position of the secondary vertex.

Chapter 5

Appendix

A Appendix A

Starting with the proof that $dyp_{\perp}dp_{\perp}d\phi_p = dy m_{\perp}dm_{\perp}d\phi_p$, in fact $m_{\perp} = \sqrt{m^2 + p_{\perp}^2}$ so $\frac{dm_{\perp}}{dp_{\perp}} = \frac{p_{\perp}}{\sqrt{m^2 + p_{\perp}^2}} = \frac{p_{\perp}}{m_{\perp}}$ and the result follow immediately.

For the other equation starting from 2.8 and inserting 2.2 one get

$$\begin{aligned} \frac{dN_i}{dy m_{\perp} dm_{\perp} d\phi_p} &= \frac{g_i}{(2\pi)^3} \sum_{n=1}^{\infty} (\pm)^n \int d^2 r_{\perp} \tau_f e^{n\mu_i/T} e^{n\gamma_{\perp} v_{\perp} \cdot p_{\perp}} \\ &\quad \int_{-\infty}^{+\infty} d\eta (m_{\perp} \cosh(y - \eta) - \vec{p}_{\perp} \cdot \nabla_{\perp} \tau_f) e^{-n\gamma_{\perp} m_{\perp} \cosh(y - \eta)/T} \\ &= \frac{g_i}{(2\pi)^3} \sum_{n=1}^{\infty} (\pm)^n \int d^2 r_{\perp} \tau_f e^{n\mu_i/T} e^{n\gamma_{\perp} v_{\perp} \cdot p_{\perp}} \\ &\quad \left(m_{\perp} K_1 \left(nm_{\perp} \frac{\gamma_{\perp}(\vec{r}_{\perp})}{T(\vec{r}_{\perp})} \right) - \vec{p}_{\perp} \cdot \nabla_{\perp} \tau_f K_0 \left(nm_{\perp} \frac{\gamma_{\perp}(\vec{r}_{\perp})}{T(\vec{r}_{\perp})} \right) \right) \end{aligned} \quad (1)$$

Where the modified Bessel function enters the game. The azimuthal integral can thus be done analytically

$$\begin{aligned} \frac{dN_i}{dy m_{\perp} dm_{\perp}} &= \frac{g_i}{\pi^2} \sum_{n=1}^{\infty} (\pm)^n \int_0^{\infty} r_{\perp} dr_{\perp} \tau_f e^{n\mu_i/T} \\ &\quad \left(m_{\perp} K_1 \left(nm_{\perp} \frac{\gamma_{\perp}(\vec{r}_{\perp})}{T(\vec{r}_{\perp})} \right) I_0 \left(n \frac{p_{\perp} v_{\perp} \gamma_{\perp}}{T} \right) \right. \\ &\quad \left. - p_{\perp} \frac{\partial \tau_f}{\partial r_{\perp}} K_0 \left(nm_{\perp} \frac{\gamma_{\perp}(\vec{r}_{\perp})}{T(\vec{r}_{\perp})} \right) I_1 \left(n \frac{p_{\perp} v_{\perp} \gamma_{\perp}}{T} \right) \right) \end{aligned} \quad (2)$$

And finally, defining $v_{\perp} = \tanh(\rho)$ and $\eta(\vec{r}_{\perp}) = \tau_f e^{n\mu_i/T}$, one obtains

$$\frac{dN_i}{dy m_\perp dm_\perp d\phi_p} = \frac{g_i}{\pi} \int_0^\infty r_\perp dr_\perp n_i(r_\perp) \left[m_\perp K_1 \left(\frac{m_\perp \cosh(\rho(r_\perp))}{T(r_\perp)} \right) I_0 \left(\frac{p_\perp \sinh(\rho(r_\perp))}{T(r_\perp)} \right) - p_\perp \frac{\partial \tau_f}{\partial r_\perp} K_0 \left(\frac{m_\perp \cosh(\rho(r_\perp))}{T(r_\perp)} \right) I_1 \left(\frac{p_\perp \sinh(\rho(r_\perp))}{T(r_\perp)} \right) \right] \quad (3)$$

B Appendix B

Under free-streaming the phase space distribution evolves as

$$f(\vec{r}, \vec{p}, t) = f(\vec{r} - \frac{\vec{p}}{E}(t - t_0), \vec{p}, t) \quad (4)$$

Using a Gaussian parametrization for the initial phase-space distribution of produced secondary particles

$$f(\vec{r}, \vec{p}, \tau) = e^{-\frac{x^2}{2R_x^2} - \frac{y^2}{2R_y^2} - \frac{p_x^2 + p_y^2}{2(\Delta\tau)^2}} \quad (5)$$

where $\Delta t = t - t_0$ and R_x R_y are the fireball radius in the indicate direction, so writing the Eq 2.17 in integral form.

$$\epsilon_x(t_0 + \Delta T) \approx \frac{\int d^2r r^2 \cos(2\psi_r \int d^3p f(\vec{r}, \vec{p}, \tau))}{\int d^2r r^2 \int d^3p f(\vec{r}, \vec{p}, \tau)} \approx \frac{R_x^2 + R_y^2}{R_x^2 + R_y^2 + 2(c\Delta\tau)^2} \quad (6)$$

introducing the initial deformation δ is possible to rewrite $R_x = \langle \vec{r}^2 \rangle_{\tau_0} (1 - \delta)$ $R_y = \langle \vec{r}^2 \rangle_{\tau_0} (1 + \delta)$ such that $\epsilon_x(t_0) = 2\delta/(1 + \delta^2)$. One get

$$\frac{\epsilon_x(t_0 + \Delta T)}{\epsilon_x(\tau_0)} = \left[1 + \frac{(c\Delta\tau)^2}{\langle \vec{r}^2 \rangle_{\tau_0}} \right]^{-1} \quad (7)$$

C Appendix C

For get the gran canonical partition function starting from Eq 2.24 visible below.

$$\ln Z_i(T, V, \mu_i) = \frac{\Delta V g_i}{2\pi^2 \hbar^3} \int_0^\infty \theta_i p^2 dp \ln(1 + \theta_i e^{\beta(\mu_i - E)}) \quad (8)$$

replacing the logarithm with taylor expansion under the assumption that $e^{\beta(\mu_i - E)} < 1 \rightarrow \mu_i < E$ and using $\lambda_i = e^{\beta\mu_i}$ it's possible to rewrite 2.2.

$$\ln Z_i(T, V, \mu_i) = \frac{\Delta V g_i}{2\pi^2 \hbar^3} \sum_K \frac{(\theta \lambda_i)^k}{k} \int_0^\infty p^2 dp e^{-k\beta E} \quad (9)$$

integrating by part

$$\ln Z_i(T, V, \mu_i) = \frac{\Delta V g_i}{2\pi^2 \hbar^3} \sum_K \frac{(\theta \lambda_i)^k}{k} \left[\frac{p^3 e^{-k\beta E}}{3} \right]_0^\infty + \int_0^\infty dp \frac{p^3 k \beta e^{-k\beta E}}{3} \frac{dE}{dp} \quad (10)$$

The first integrand vanish.

$$\frac{dE}{dp} = \frac{d}{dp} (\sqrt{p^2 + m_i^2}) = \frac{p}{\sqrt{p^2 + m_i^2}} = \frac{p}{E} \quad (11)$$

so

$$\ln Z_i(T, V, \mu_i) = \frac{\Delta V g_i}{2\pi^2 \hbar^3} \sum_K \frac{(\theta \lambda_i)^k}{k} \int_0^\infty dp \frac{p^3 k \beta e^{-k\beta E}}{3} \frac{E}{p} \quad (12)$$

introducing $x = k\beta E$, $w_i = k\beta m_i$ and $y_i = x/w_i$

$$\ln Z_i(T, V, \mu_i) = \frac{\Delta V g_i}{2\pi^2 \hbar^3} \sum_K \frac{(\theta \lambda_i)^k}{k} \int_0^\infty dE \frac{p^3 k \beta e^{-k\beta}}{3} \quad (13)$$

$$\ln Z_i(T, V, \mu_i) = \frac{\Delta V g_i}{2\pi^2 \hbar^3} \sum_K \frac{(\theta \lambda_i)^k}{k} \int_0^\infty dE \frac{(E^2 - m_i^2)^{3/2} k \beta e^{-k\beta}}{3} \quad (14)$$

$$\ln Z_i(T, V, \mu_i) = \frac{\Delta V g_i m_i^2}{2\pi^2 \hbar^3 \beta} \sum_K \frac{(\theta \lambda_i)^k}{k^2} \int_0^\infty dE \frac{(x^2 - w_i^2)^{3/2}}{3w_i^2} e^{-x} \quad (15)$$

$$\ln Z_i(T, V, \mu_i) = \frac{\Delta V g_i m_i^2}{6\pi^2 \hbar^3 \beta} \sum_K \frac{(\theta \lambda_i)^k w_i}{k^2} \int_0^\infty dE \left(\frac{x^2}{w_i^2} - 1 \right)^{3/2} e^{-x} \quad (16)$$

$$\ln Z_i(T, V, \mu_i) = \frac{\Delta V g_i m_i^2}{6\pi^2 \hbar^3 \beta} \sum_K \frac{(\theta \lambda_i)^k w_i}{k^2} \int_0^\infty dE w_i (y^2 - 1)^{3/2} e^{-w_i y} \quad (17)$$

introducing the modified Bessel function

$$k_2(q) = \frac{q^2}{3} \int_0^\infty dy (y^2 - 1)^{3/2} e^{-qy} \quad (18)$$

and finally

$$\ln Z_i(T, V, \mu_i) = \frac{\Delta V g_i}{2\pi^2 \hbar^3 \beta} \sum_K \frac{(\theta_i e^{\beta \mu_i})^k}{k^2} m_i^2 K_2(k\beta m_i) \quad (19)$$

Bibliography

- [1] Fernando Quevedo and Andreas Schachner. *Cambridge Lectures on The Standard Model*. 2024. arXiv: 2409.09211 [hep-th]. URL: <https://arxiv.org/abs/2409.09211>.
- [2] P. Skands. “Introduction to QCD”. In: *Searching for New Physics at Small and Large Scales*. WORLD SCIENTIFIC, Sept. 2013. DOI: 10.1142/9789814525220_0008. URL: http://dx.doi.org/10.1142/9789814525220_0008.
- [3] Alexandre Obertelli and Hiroyuki Sagawa. “Modern Nuclear Physics”. In: *Springer Singapore* (2021). ISSN: 2198-7882. DOI: <https://doi.org/10.1007/978-981-16-2289-2>.
- [4] Nicola Semprini Cesaro. *Fisica Subnucleare*. 2024.
- [5] H David Politzer. “Asymptotic freedom: An approach to strong interactions”. In: *Physics Reports* 14.4 (1974), pp. 129–180. ISSN: 0370-1573. DOI: [https://doi.org/10.1016/0370-1573\(74\)90014-3](https://doi.org/10.1016/0370-1573(74)90014-3). URL: <https://www.sciencedirect.com/science/article/pii/0370157374900143>.
- [6] Michael E. Peskin and Daniel V. Schroeder. *An Introduction to quantum field theory*. Reading, USA: Addison-Wesley, 1995. DOI: 10.1201/9780429503559.
- [7] Sarah Herrmann. “Measurements of forward charged-particle multiplicity and multiplicity dependence of forward J/Ψ production in pp collisions with the ALICE experiment at LHC”. Presented 24 Oct 2024. U. Lyon 1, IUT, 2024. URL: <https://cds.cern.ch/record/2920632>.
- [8] Ulrich W. Heinz. *Concepts of Heavy-Ion Physics*. 2004. arXiv: hep-ph/0407360 [hep-ph]. URL: <https://arxiv.org/abs/hep-ph/0407360>.
- [9] S. Acharya et al. “Measurements of Chemical Potentials in Pb-Pb Collisions at $\sqrt{s} = 5.02$ TeV”. In: *Physical Review Letters* 133.9 (Aug. 2024). ISSN: 1079-7114. DOI: 10.1103/physrevlett.133.092301. URL: <http://dx.doi.org/10.1103/PhysRevLett.133.092301>.

- [10] J. D. Bjorken. “Highly relativistic nucleus-nucleus collisions: The central rapidity region”. In: *Phys. Rev. D* 27 (1 1983), pp. 140–151. DOI: 10.1103/PhysRevD.27.140. URL: <https://link.aps.org/doi/10.1103/PhysRevD.27.140>.
- [11] Nicolo Jacazio. “Production and nuclear modification factors of pions, kaons and protons in pp and AA collisions at the LHC”. PhD thesis. alma, 2019. URL: <http://amsdottorato.unibo.it/9036/>.
- [12] Zoltán Fodor. “The QCD Phase Diagram and Equation of State”. In: *ELEMENTARY PARTICLE PHYSICS* (Feb. 2021). URL: <https://www.gauss-centre.eu/results/elementaryparticlephysics/the-qcd-phase-diagram-and-equation-of-state>.
- [13] Bikash Sinha. “Hawking radiation from strange quark nuggets, relics of the QCD phase transition”. In: *Phys. Rev. D* 101 (10 2020), p. 103007. DOI: 10.1103/PhysRevD.101.103007. URL: <https://link.aps.org/doi/10.1103/PhysRevD.101.103007>.
- [14] Sonali Padhan. “Multiplicity and energy dependence of $\Lambda(1520)$ production in pp collisions at $\sqrt{s} = 5.02$ and 13 TeV with ALICE at the LHC”. Presented 29 Jan 2025. Indian Inst. Tech., Mumbai, 2025. URL: <https://cds.cern.ch/record/2924203>.
- [15] Carolina Arata. “Measurement of isolated photon-hadron correlations in Pb–Pb collisions at 5.02 TeV with the ALICE experiment at LHC”. Presented 08 Oct 2024. U. Grenoble Alpes, 2024. URL: <https://cds.cern.ch/record/2922803>.
- [16] ”Mattia”. *Evolution of collisions and QGP*. URL: <https://particlesandfriends.wordpress.com/2016/10/14/evolution-of-collisions-and-qgp/#respond>.
- [17] Michael L. Miller et al. “Glauber Modeling in High-Energy Nuclear Collisions”. In: *Annual Review of Nuclear and Particle Science* 57.1 (Nov. 2007), pp. 205–243. ISSN: 1545-4134. DOI: 10.1146/annurev.nucl.57.090506.123020. URL: <http://dx.doi.org/10.1146/annurev.nucl.57.090506.123020>.
- [18] Golam Sarwar. “Evolution of Perturbation in a Hydrodynamically Expanding System Formed in Relativistic Heavy Ion Collision”. PhD thesis. Aug. 2018. DOI: 10.13140/RG.2.2.10003.53284.
- [19] Raimond Snellings. “Elliptic flow: a brief review”. In: *New Journal of Physics* 13.5 (2011), p. 055008. DOI: 10.1088/1367-2630/13/5/055008. URL: <https://dx.doi.org/10.1088/1367-2630/13/5/055008>.
- [20] D. Oliinychenko, P. Huovinen, and H. Petersen. “Cooper-Frye Negative Contributions in a Coarse-Grained Transport Approach”. In: *Journal of Physics: Conference Series* 599 (Dec. 2014). DOI: 10.1088/1742-6596/599/1/012017.

- [21] D. Teaney, J. Lauret, and E. V. Shuryak. *A Hydrodynamic Description of Heavy Ion Collisions at the SPS and RHIC*. 2001. arXiv: nucl-th/0110037 [nucl-th]. URL: <https://arxiv.org/abs/nucl-th/0110037>.
- [22] Peter F. Kolb, Josef Sollfrank, and Ulrich Heinz. “Anisotropic transverse flow and the quark-hadron phase transition”. In: *Physical Review C* 62.5 (Oct. 2000). ISSN: 1089-490X. DOI: 10.1103/physrevc.62.054909. URL: <http://dx.doi.org/10.1103/PhysRevC.62.054909>.
- [23] Peter F. Kolb and Ulrich Heinz. *Hydrodynamic description of ultrarelativistic heavy-ion collisions*. 2003. arXiv: nucl-th/0305084 [nucl-th]. URL: <https://arxiv.org/abs/nucl-th/0305084>.
- [24] F. Becattini. *An introduction to the Statistical Hadronization Model*. 2009. arXiv: 0901.3643 [hep-ph]. URL: <https://arxiv.org/abs/0901.3643>.
- [25] Anton Andronic et al. “The multiple-charm hierarchy in the statistical hadronization model”. In: *Journal of High Energy Physics* 2021 (July 2021). DOI: 10.1007/JHEP07(2021)035.
- [26] A. Keränen and F. Becattini. “Chemical factors in canonical statistical models for relativistic heavy ion collisions”. In: *Phys. Rev. C* 65 (4 2002), p. 044901. DOI: 10.1103/PhysRevC.65.044901. URL: <https://link.aps.org/doi/10.1103/PhysRevC.65.044901>.
- [27] A Andronic et al. “Hadron yields, the chemical freeze-out and the QCD phase diagram”. In: *Journal of Physics: Conference Series* 779 (Jan. 2017), p. 012012. ISSN: 1742-6596. DOI: 10.1088/1742-6596/779/1/012012. URL: <http://dx.doi.org/10.1088/1742-6596/779/1/012012>.
- [28] A. Andronic, P. Braun-Munzinger, and J. Stachel. “Hadron production in central nucleus–nucleus collisions at chemical freeze-out”. In: *Nuclear Physics A* 772.3–4 (June 2006), pp. 167–199. ISSN: 0375-9474. DOI: 10.1016/j.nuclphysa.2006.03.012. URL: <http://dx.doi.org/10.1016/j.nuclphysa.2006.03.012>.
- [29] Anton Andronic et al. “The multiple-charm hierarchy in the statistical hadronization model”. In: *Journal of High Energy Physics* 2021.7 (July 2021). ISSN: 1029-8479. DOI: 10.1007/jhep07(2021)035. URL: [http://dx.doi.org/10.1007/JHEP07\(2021\)035](http://dx.doi.org/10.1007/JHEP07(2021)035).
- [30] Hideki YUKAWA. “On the Interaction of Elementary Particles. I”. In: *Proceedings of the Physico-Mathematical Society of Japan. 3rd Series* 17 (1935), pp. 48–57. DOI: 10.11429/ppmsj1919.17.0_48.

- [31] Arthur I. Miller. “Werner Heisenberg and the Beginning of Nuclear Physics”. In: *Physics Today* 38.11 (Nov. 1985), pp. 60–68. ISSN: 0031-9228. DOI: 10.1063/1.880993. eprint: https://pubs.aip.org/physicstoday/article-pdf/38/11/60/7420012/60_1_online.pdf. URL: <https://doi.org/10.1063/1.880993>.
- [32] Morris Low. “Shoichi Sakata: His Life, the Sakata Model and His Achievements”. In: *Progress of Theoretical Physics Supplement* 167 (Feb. 2007). DOI: 10.1143/PTPS.167.1.
- [33] J. J. de Swart, P. M. M. Maessen, and TH. A. Rijken. *The One-Boson-Exchange Potential Model Approach*. 1994. arXiv: nucl-th/9405008 [nucl-th]. URL: <https://arxiv.org/abs/nucl-th/9405008>.
- [34] H. Garcilazo, A. Valcarce, and T. F. Caramés. “Charmed baryon–nucleon interaction”. In: *The European Physical Journal C* 79.7 (July 2019). ISSN: 1434-6052. DOI: 10.1140/epjc/s10052-019-7110-z. URL: <http://dx.doi.org/10.1140/epjc/s10052-019-7110-z>.
- [35] Saori Maeda et al. “A model of charmed baryon–nucleon potential and two- and three-body bound states with charmed baryon”. In: *Progress of Theoretical and Experimental Physics* 2016.2 (Feb. 2016), p. 023D02. ISSN: 2050-3911. DOI: 10.1093/ptep/ptv194. URL: <http://dx.doi.org/10.1093/ptep/ptv194>.
- [36] A Valcarce et al. “Quark-model study of few-baryon systems”. In: *Reports on Progress in Physics* 68.5 (Mar. 2005), pp. 965–1041. ISSN: 1361-6633. DOI: 10.1088/0034-4885/68/5/r01. URL: <http://dx.doi.org/10.1088/0034-4885/68/5/R01>.
- [37] Jan Smit. “Chiral symmetry”. In: *Introduction to Quantum Fields on a Lattice*. Cambridge Lecture Notes in Physics. Cambridge University Press, 2023, pp. 193–228.
- [38] Takaya Miyamoto et al. “ Λ_c N interaction from lattice QCD and its application to Λ_c c hypernuclei”. In: *Nuclear Physics A* 971 (2018), pp. 113–129. ISSN: 0375-9474. DOI: <https://doi.org/10.1016/j.nuclphysa.2018.01.015>. URL: <https://www.sciencedirect.com/science/article/pii/S0375947418300228>.
- [39] S. Navas et al. “Review of particle physics”. In: *Phys. Rev. D* 110.3 (2024), p. 030001. DOI: 10.1103/PhysRevD.110.030001.
- [40] C. Van Der Leun and C. Alderliesten. “The deuteron binding energy”. In: *Nuclear Physics A* 380.2 (1982), pp. 261–269. ISSN: 0375-9474. DOI: [https://doi.org/10.1016/0375-9474\(82\)90105-1](https://doi.org/10.1016/0375-9474(82)90105-1). URL: <https://www.sciencedirect.com/science/article/pii/0375947482901051>.

- [41] Volodymyr Vovchenko and Horst Stoecker. “Thermal-FIST: A package for heavy-ion collisions and hadronic equation of state”. In: *Computer Physics Communications* 244 (Nov. 2019), pp. 295–310. ISSN: 0010-4655. DOI: 10.1016/j.cpc.2019.06.024. URL: <http://dx.doi.org/10.1016/j.cpc.2019.06.024>.
- [42] Stella Biderman et al. *Pythia: A Suite for Analyzing Large Language Models Across Training and Scaling*. 2023. arXiv: 2304.01373 [cs.CL]. URL: <https://arxiv.org/abs/2304.01373>.
- [43] ALICE Collaboration. *Letter of intent for ALICE 3: A next-generation heavy-ion experiment at the LHC*. 2022. arXiv: 2211.02491 [physics.ins-det]. URL: <https://arxiv.org/abs/2211.02491>.
- [44] Cern webpage. *ALICE*. URL: <https://home.cern/science/experiments/alice>.
- [45] Elena Botta. “Particle identification performance at ALICE”. In: *5th Large Hadron Collider Physics Conference*. Sept. 2017. arXiv: 1709.00288 [nucl-ex].
- [46] ALICE collaboration. “Alignment of the ALICE Inner Tracking System with cosmic-ray tracks”. In: *Journal of Instrumentation* 5.03 (Mar. 2010), P03003–P03003. ISSN: 1748-0221. DOI: 10.1088/1748-0221/5/03/P03003. URL: <http://dx.doi.org/10.1088/1748-0221/5/03/P03003>.
- [47] Tiantian Cheng. “Measurements of charm-strange baryon production with ALICE at the LHC”. Presented 27 May 2024. Hua-Zhong Normal U., 2024. URL: <https://cds.cern.ch/record/2908766>.
- [48] Luigi Rolandi, Werner Riegler, and Walter Blum. *Particle Detection with Drift Chambers*. Particle Acceleration and Detection. Springer, 2008. DOI: 10.1007/978-3-540-76684-1.
- [49] G Dellacasa et al. *ALICE time projection chamber: Technical Design Report*. Technical design report. ALICE. Geneva: CERN, 2000. URL: <https://cds.cern.ch/record/451098>.
- [50] David Rohr et al. “ALICE HLT TPC Tracking of Pb-Pb Events on GPUs”. In: *Journal of Physics: Conference Series* (2012). URL: <https://dx.doi.org/10.1088/1742-6596/396/1/012044>.
- [51] Betty Bezverkhny Abelev et al. “Performance of the ALICE Experiment at the CERN LHC”. In: *Int. J. Mod. Phys. A* 29 (2014), p. 1430044. DOI: 10.1142/S0217751X14300440. arXiv: 1402.4476 [nucl-ex].
- [52] Cern webpage. *ALICE*. URL: https://alice-collaboration.web.cern.ch/menu_proj_items/Muon-Spect.
- [53] *Technical Design Report for the Muon Forward Tracker*. Tech. rep. 2015. URL: <https://cds.cern.ch/record/1981898>.

- [54] B. Abelev et al. “Measurement of charm production at central rapidity in proton-proton collisions at $\sqrt{s} = 2.76$ TeV”. In: *Journal of High Energy Physics* 2012.7 (July 2012). ISSN: 1029-8479. doi: 10.1007/jhep07(2012)191. URL: [http://dx.doi.org/10.1007/JHEP07\(2012\)191](http://dx.doi.org/10.1007/JHEP07(2012)191).